

# Chapter 4

## Synthetic examples

In chapter 3, I developed formulations for regularized data-domain and image-domain joint inversion of time-lapse data sets. In this chapter, I present applications of these methods to synthetic data sets. These carefully designed synthetic examples represent various time-lapse imaging problems where it is difficult to apply the conventional methods described in chapter 2.

This chapter is divided into two broad sections:

1. Data-domain inversion: Using a two-dimensional model derived from the Marmousi model (Bourgeois et al., 1991), I show that regularized joint data-domain inversion can be used for direct imaging of simultaneous-source time-lapse data sets. Because the migration operator does not account for cross-talk between different sources, and for geometry and timing differences between simultaneous-source data sets, it generates artifacts that contaminate the time-lapse amplitudes of interest. This example shows that regularized joint data-domain inversion can attenuate these artifacts, producing images that are similar in quality to those derived from conventional data sets. In this example, image-domain inversion is not applicable because the Hessian matrix of its least-squares objective function is far from being diagonal, and cannot be sufficiently approximated by its truncated form.

2. Image-domain inversion: Although image-domain inversion is not readily applicable to the example described above, it can be applied to several practical time-lapse imaging problems. As discussed in chapter 3, one advantage of image-domain inversion is that it can be easily solved in a target-oriented manner. In this section, I demonstrate that target-oriented regularized joint image-domain inversion can be used to correct for distortions and artifacts in time-lapse images caused by:

- *Poor and Irregular illumination due to complex overburden.* Using a two-dimensional sub-salt model modified from the SEAM model (Fehler and Larner, 2008), I show that, even for perfectly repeated geometries, the time-lapse image in reservoirs under complex overburden can be strongly distorted. I demonstrate that regularized joint inversion can correct for such distortions, thereby providing a more reliable time-lapse image.
- *Non-repeated geometries due to obstructions in monitor acquisition.* I present two examples that show how regularized joint inversion can be used to correct for acquisition differences between seismic surveys.
  - Using a two-dimensional model modified from the SEAM model (Fehler and Larner, 2008), I show how joint inversion can be used to correct for artifacts in time-lapse images caused by obstructions in the geometry of the monitoring survey.
  - Using a three-dimensional synthetic model derived by convolving Hessian matrices from three ocean-bottom-cable (OBC) field-data geometries (discussed in chapter 5) with carefully designed time-lapse reflectivity models. Furthermore, I demonstrate how different regularization parameters in the inversion affect the quality of time-lapse images. Because image-domain is relatively computationally inexpensive, it is possible to test different plausible regularization parameters in near real-time.

These synthetic examples show that regularized joint inversion provides better quality time-lapse images than conventional imaging by migration.

## DATA-DOMAIN INVERSION

In this section, I describe an application of data-domain inversion to synthesized *field-encoded* simultaneous-source data sets. First, I discuss the concept of acquiring seismic data with simultaneous sources and how this can be advantageous to time-lapse seismic imaging. I also discuss how acquiring data this way may lead to discrepancies that will contaminate production-related time-lapse amplitude signals. I then apply the data-domain inversion method developed in chapter 3 to synthesized simultaneous-source time-lapse data with non-repeated source geometries and non-repeated relative shot times.

### *Example I: Inversion of simultaneous-source time-lapse data*

Conventional seismic data acquisition involves a single seismic source and a recording array of receivers. Although it is not a new idea (Womack et al., 1990), recent advances in acquisition technology enable seismic acquisition with multiple sources (Hampson et al., 2008; Beasley, 2008). This acquisition approach, also called simultaneous shooting (or multi-shooting, or blended acquisition), can be used to achieve longer offsets, better shot-sampling, and improved time and cost efficiency (van Mastriigt et al., 2002; Berkhout et al., 2008; Howe et al., 2009). The recorded data can be separated into independent shot records and then imaged with conventional methods (Hampson et al., 2008; Spitz et al., 2008; Ikelle, 2009; Ayeni et al., 2011), or they can be imaged directly without separation (Berkhout et al., 2008; Tang and Biondi, 2009; Ayeni et al., 2009).

Although time-lapse seismic imaging is an established technology for monitoring hydrocarbon reservoirs, it still has several limitations. First, because of the high cost of conventional (single-source) acquisition, it is impractical to have short time intervals between surveys. Therefore, typical time-intervals between monitoring surveys may be too large to measure production-related, short-period variations in reservoir properties. Because of the large time intervals between conventional time-lapse seismic surveys, it may be difficult to match time-lapse seismic signatures to changes

in reservoir properties derived from temporally continuously-sampled sources (e.g., production data).

Secondly, in many time-lapse seismic applications, inaccuracies in the replication of acquisition geometries for different surveys (*geometry non-repeatability*) is a recurring problem. Although modern acquisition techniques can improve repeatability of shot-receiver geometries, field conditions usually prevent perfect repetition. As discussed in previous chapters, in order to correctly interpret differences in time-lapse seismic images that are caused by changes in reservoir properties, non-repeatability effects must be removed.

Thirdly, because of operational, climatic, and other limitations, the acquisition time-window may be too small for conventional seismic data acquisition. In such cases, it would be difficult to acquire conventional seismic data sets at desirable intervals.

Some limitations in current and conceptual time-lapse seismic applications can be overcome by simultaneous-source acquisition. First, acquiring time-lapse data sets with multiple seismic sources can reduce acquisition time and cost, making it possible to acquire more data sets at shorter time intervals. Sufficiently small survey intervals will enable *quasi-continuous* monitoring of changes in reservoir properties. Other methods for quasi-continuous monitoring have been suggested (Arogunmati and Harris, 2009). Secondly, the ability to account for differences in survey geometries during imaging makes repetition of survey geometries unnecessary. Furthermore, because of its high efficiency, simultaneous-source acquisition can be used for seasonal time-lapse seismic data acquisition in areas with short acquisition time-windows (Berkhout, 2008). Depending on operational limitations, an arbitrary number of seismic sources can be used for each survey.

There are two sources of discrepancies in time-lapse seismic data sets recorded with multiple sources, namely, geometry and shot-timing non-repeatabilities (Ayeni et al., 2009). As mentioned above, geometry non-repeatability is a result of differences in acquisition geometries for different surveys. Shot-timing non-repeatability between

different surveys is a result of mismatches in their relative shooting times. Neglecting survey geometry and shot-timing repeatability during acquisition ensures time and cost efficiency. However, if not accounted for, these two discrepancies will degrade the resulting time-lapse seismic images. Because conventional imaging and time-lapse processing methods are inadequate to account for such discrepancies, I apply the data-domain inversion method developed in the previous chapter (equation 3.52). Data-domain phase-encoded inversion removes discrepancies between different surveys and provides reliable estimates of the time-lapse amplitude changes. In addition, this method avoids the cost of separating the acquired data into individual records.

For this problem, the image-domain formulation is not applicable. This is because, as shown by Tang (2008), the Hessian matrix of the objective function of simultaneous-source data-fitting problem is far from being diagonal. Therefore, in this example, the truncated target-oriented Hessian (defined in equation 3.10) is a poor approximation of the full Hessian matrix. Because it is impractical to compute the full Hessian for any realistic imaging problem, a data-domain formulation is more appropriate in this example.

In the next section, I discuss linear phase-encoded modeling of simultaneous-source data sets.

## Linear phase-encoded modeling and simultaneous-shooting

From the linearized Born modeling equation in equation 3.1, the recorded data due to shots starting from  $s = q$  to  $s = p$  is given by

$$d(\mathbf{x}_{spq}, \mathbf{x}_r, \omega) = \sum_{s=p}^q a(\gamma_s) \omega^2 \sum_{\mathbf{x}} f_s(\omega) G(\mathbf{x}_s \mathbf{x}, \omega) G(\mathbf{x}, \mathbf{x}_r, \omega) m(\mathbf{x}), \quad (4.1)$$

where  $a(\gamma_s)$  is

$$a(\gamma_s) = e^{i\gamma_s} = e^{i\omega t_s}, \quad (4.2)$$

and  $\gamma_s$ , the time-delay function, depends on the delay time  $t_s$  at shot  $s$ .

For acquisition efficiency, it is unnecessary to repeat either the acquisition geometry or the relative shot timings for different surveys. By eliminating the cost associated with ensuring repeatability between surveys, the total acquisition cost can be reduced significantly. Because acquisition cost is usually several times higher than the processing cost, a reduction in acquisition cost will significantly reduce the total seismic monitoring cost. In addition, further cost reduction is achieved by imaging all the data sets directly.

Figure 4.1 shows examples of wavefields from two configurations of simultaneous-shooting. In both figures, the third dimension represents the survey time, while the orthogonal lines indicate positions of the displayed slices within the image cube.

## Regularized phase-encoded joint inversion

To perform regularized phase-encoded inversion, the data-domain RJMI formulation in equation 3.52 is modified as follows:

$$S(\mathbf{m}_0, \dots, \mathbf{m}_n) = \sum_{i=0}^n \left\| \tilde{\mathbf{L}}_i \mathbf{m}_i - \tilde{\mathbf{d}}_i \right\|^2 + \sum_{i=0}^n \|\epsilon_i \mathbf{A}_i \mathbf{m}_i\|^2 + \sum_{i=1}^n \|\zeta_i \mathbf{\Lambda}_i(\mathbf{m}_{i-1}, \mathbf{m}_i)\|^2, \quad (4.3)$$

where  $\tilde{\mathbf{d}}_i = \mathbf{B}_i \mathbf{L}_i \mathbf{m}_i$  is the recorded simultaneous-source data,  $\mathbf{B}$  is the encoding operator,  $\mathbf{m}$  is the earth reflectivity,  $\tilde{\mathbf{L}} = \mathbf{B}\mathbf{L}$  is the phase-encoded modeling operator in equation 4.2, and other terms are as defined in chapter 3.

The migrated image, computed by applying the adjoint operator  $\tilde{\mathbf{L}}^T$  to  $\tilde{\mathbf{d}}$ , will contain crosstalk artifacts generated by cross-correlation between incongruous source and receiver wavefields (Romero et al., 2000; Tang and Biondi, 2009). In addition, because of the associated geometry and relative shot-time non-repeatability, different surveys have unique crosstalk artifacts. As shown below, regularized phase-encoded joint inversion can attenuate these artifacts.

Because several shots are encoded and directly imaged, the computational cost of this approach is considerably reduced compared to the cost of inverting non-encoded

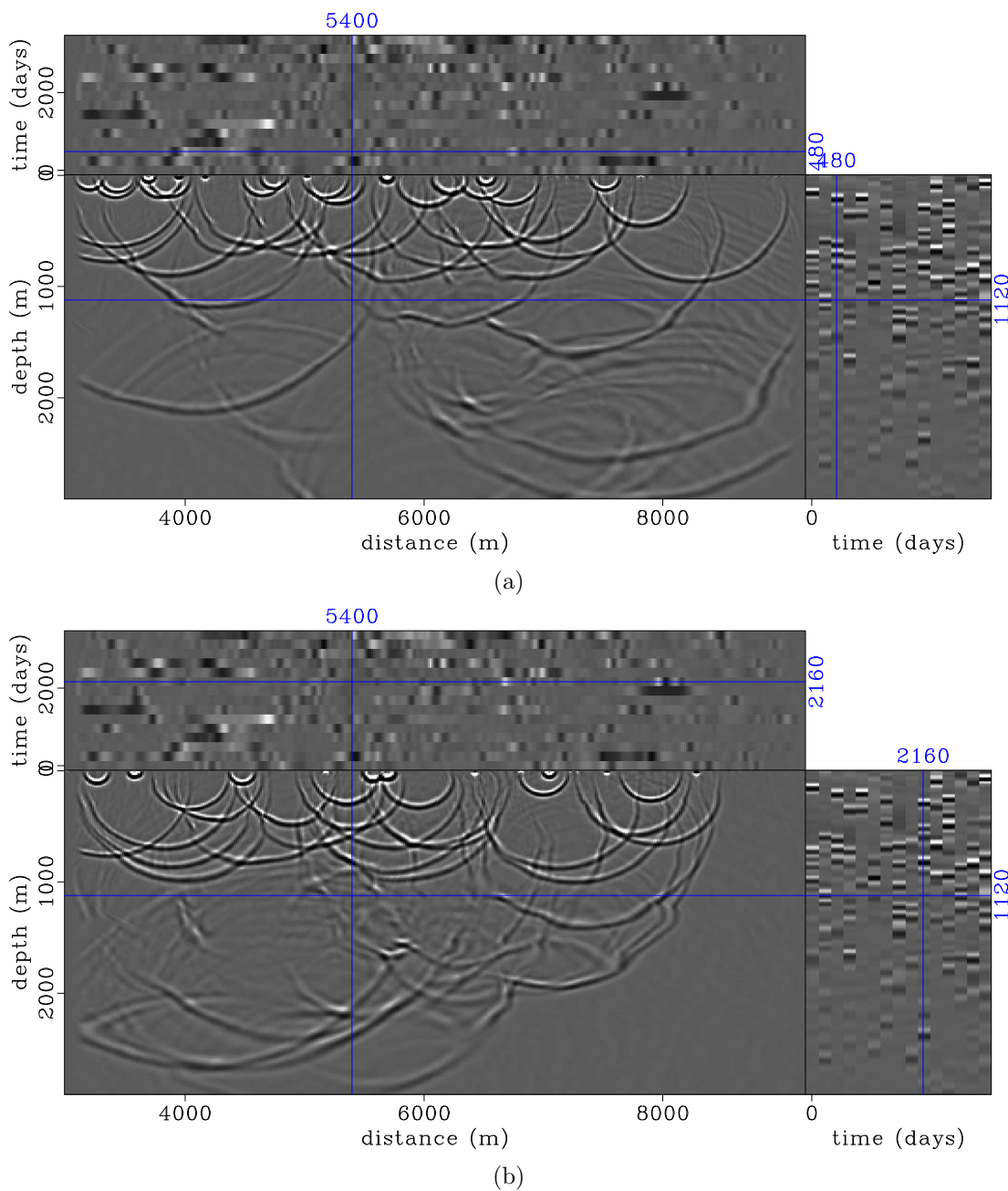


Figure 4.1: Wavefields from multiple randomized simultaneous sources (a), and from two continuously shooting seismic sources (b). In each figure, the blue line indicates intersecting positions of the the three slices that are displayed. In Panel (a), the geometry and relative shot-timing are different for all surveys, whereas in Panel (b), only the acquisition geometry differs between surveys. The third dimension denotes survey/recording time. [CR]. `chap4/. wave-dat0,wave-dat1`

data sets. Furthermore, because the data are already encoded in the field, and they are not separated prior to imaging, it is impossible to change the encoding function during iterative inversion. However, because the data sets are encoded differently, artifacts are incoherent between images.

## Example

Figure 4.2 shows a modified section of the Marmousi velocity model (Versteeg, 1994). I represent the production-related changes between surveys as changes in reflectivity within the reservoir (Figure 4.2). For simplicity, I assume that there are no geometrical changes in the overburden between the surveys. In addition, I assume that there are no changes in the background velocity.

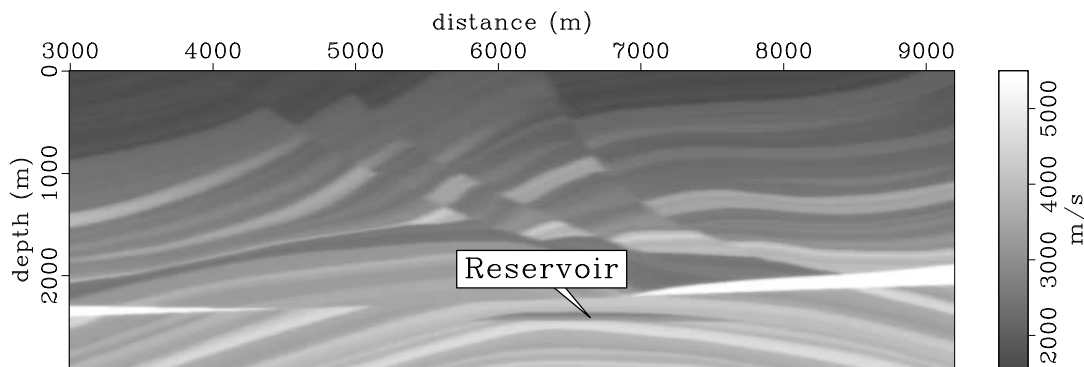


Figure 4.2: Baseline velocity model of the modified Marmousi model. The only changes between surveys are reflectivity changes within the reservoir. [CR].

chap4/. vel-0

Using these modified models, I simulate 15 simultaneous-source data sets, which represent different production stages (Figure 4.3). Each data set comprises 56 randomly encoded shot records with unique shot positions and unique relative shot-timings (Figure 4.4). The receiver spread, which covers the length of the model, is fixed for all data sets. I simulate these data using a phase-encoding one-way wave-equation operator.

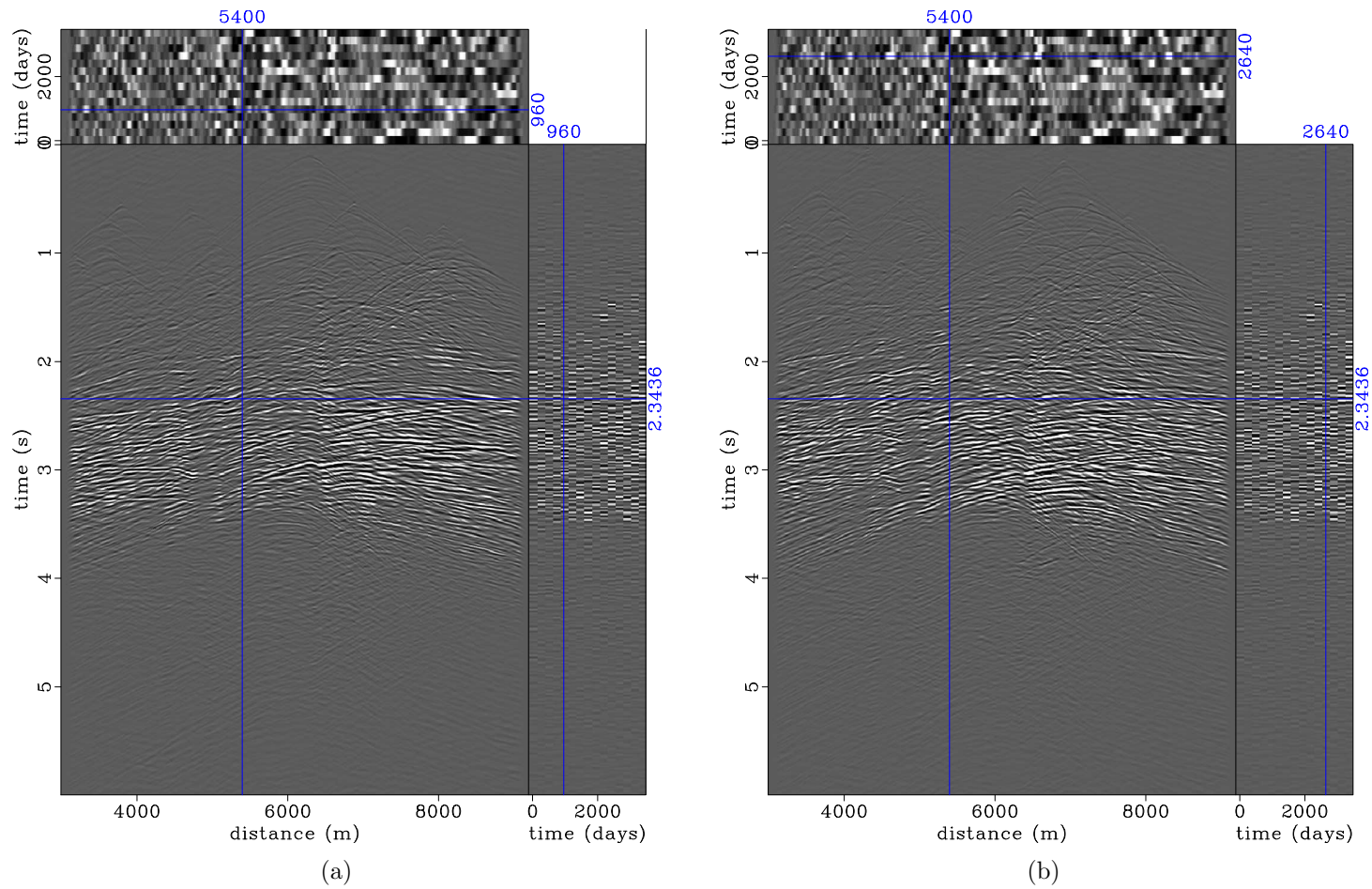


Figure 4.3: Synthetic data from multiple asynchronous sources. In (a) and (b), the front panels show the encoded data for two different surveys. In addition to varying the relative shot time, the source positions are also different for each survey (Figure 4.4). Note that, whereas the first dimension denote two-way travel time, the third dimension denotes survey/recording time. [CR]. `chap4/. tdat-10,tdat-11`

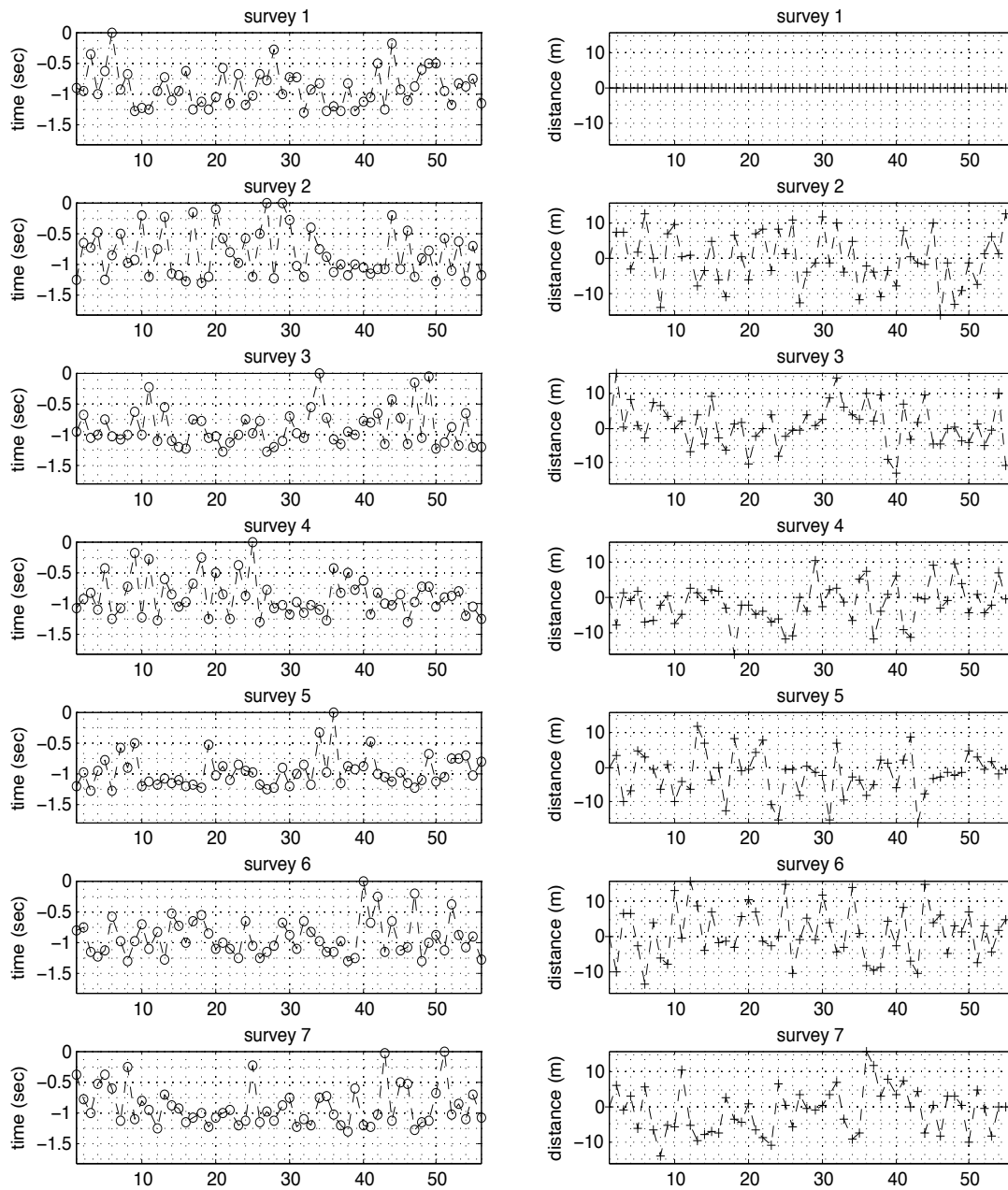


Figure 4.4: Plots of relative time-delays (left) and shot-displacements for seven out of the fifteen numerical models that were used to generate the data in Figure 4.3. In all plots, the horizontal axis indicates shot position. The relative shooting times are referenced to the earliest shot in each survey, whereas shot-displacements are referenced to the baseline shot positions. [CR]. `chap4/. source-time`

For comparison, using the same models, the same number of shots and receivers and assuming perfect repeatability, I also simulate 15 conventional single-source data sets. I image these data with the same algorithm as in the simultaneous-source case (described below), but without phase-encoding. Figure 4.5 shows the migrated images, and the corresponding time-lapse images, derived from these data.

Figure 4.6(a) shows the migrated images derived from the simultaneous-source data sets. The corresponding time-lapse images are presented in Figure 4.6(b). These results are obtained by direct imaging of the encoded data with a phase-encoded migration operator. As shown in Figure 4.6(a), compared to the reference images (Figure 4.5(a)), these migrated images—and as a consequence, the time-lapse images—are contaminated by strong non-repeatability and crosstalk artifacts. These contaminating artifacts make it difficult to relate the amplitudes in the time-lapse images (Figure 4.6(b)) to actual changes in properties within the reservoir.

Next, using the plane-wave destruction method (Fomel, 2002), I estimate the dip-field from the migrated baseline image (Figures 4.7). I assume that prior to the start of monitoring with simultaneous-source data, a reference baseline image derived from conventional (single-source) data is available. These dips are used to construct the spatial regularization operator that is used in the inversion.

In Figure 4.7, to preserve faults in image, I manually picked the faults in the migrated images and then estimate the dips along them. Furthermore, based on the locations of these faults, I define dip-contrast parameters, which depend on the distance of an image point from a fault location (Figure 4.8). To obtain these parameters, I smooth the manually picked faults with a triangular filter such that the largest values are close to the fault locations. Then, by changing the filter range at each image point according to these values, the faults are preserved during inversion. I change the filter range by modifying the spectral factorization weights (Fomel et al., 2003). In general, the filter strength reduces as its range increases, and vice versa.

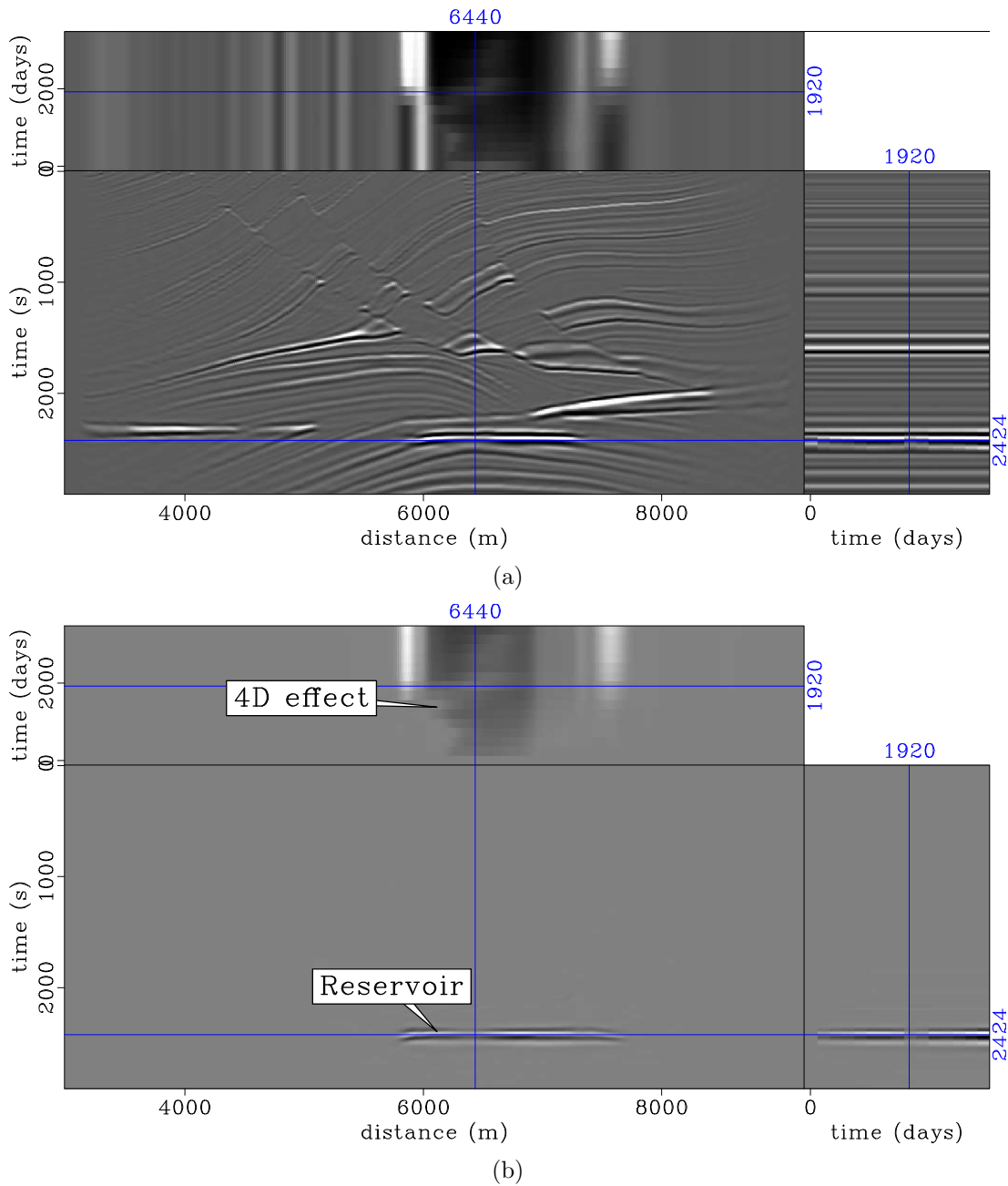


Figure 4.5: Migrated images (a) and corresponding time-lapse estimates (b) obtained from perfectly repeated conventional (single-source) data sets. In these (and in similar Figures), the side panel (third axis) shows the seismic properties (a) and time-lapse changes (b) at a fixed spatial position, whereas the top panel shows the spatial-temporal distribution seismic properties. [CR]. `chap4/. pnomig-0,pnomig4d-1`

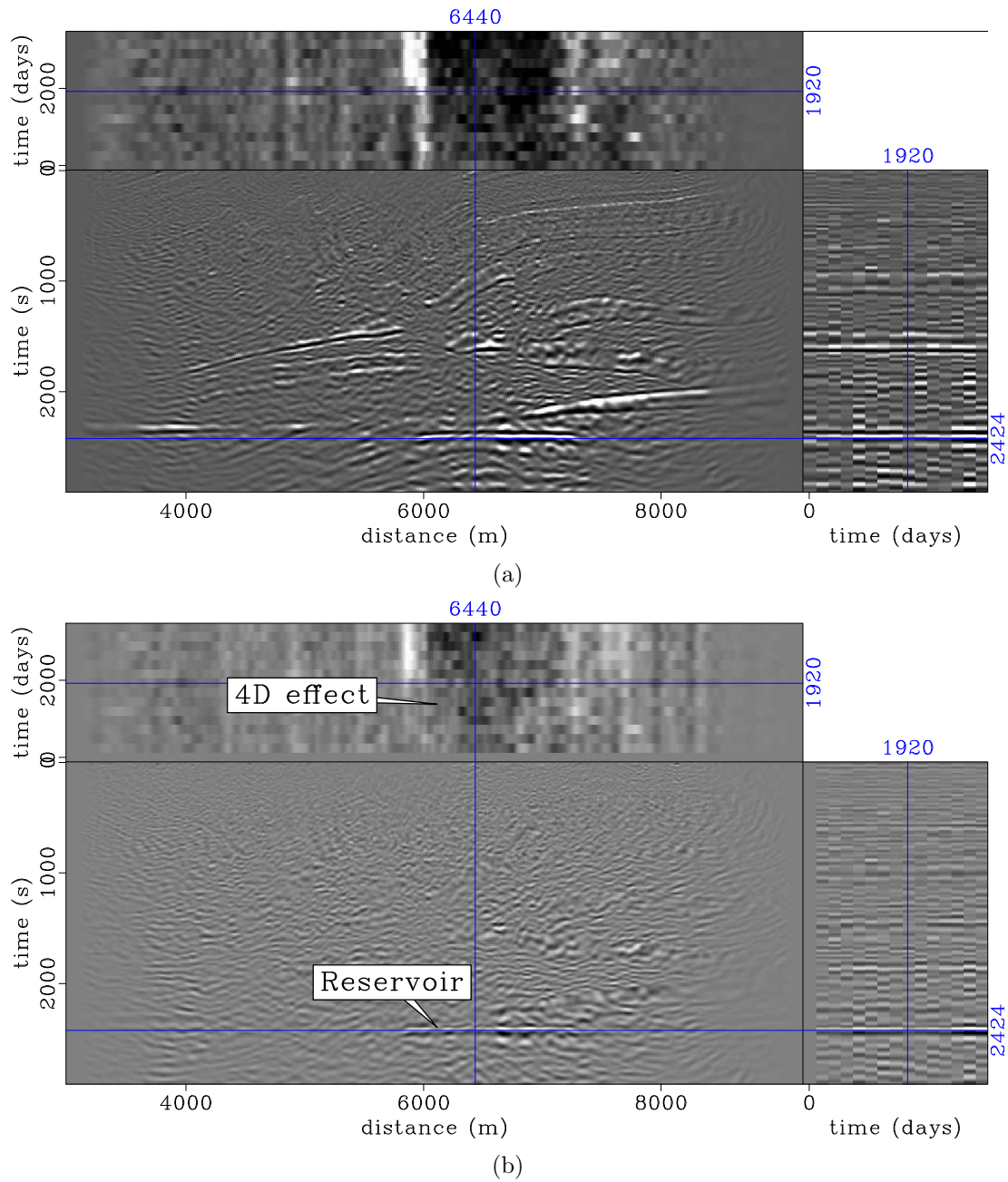


Figure 4.6: Images (a) and corresponding time-lapse estimates (b) obtained from migrating the data sets in Figure 4.3. In both Figures, note the numerous artifacts caused by geometry and shot-timing non-repeatability and crosstalk artifacts. Without attenuating these artifacts, it would be difficult to accurately interpret the time-lapse information. [CR]. chap4/. pmig-0,pmig4d-1

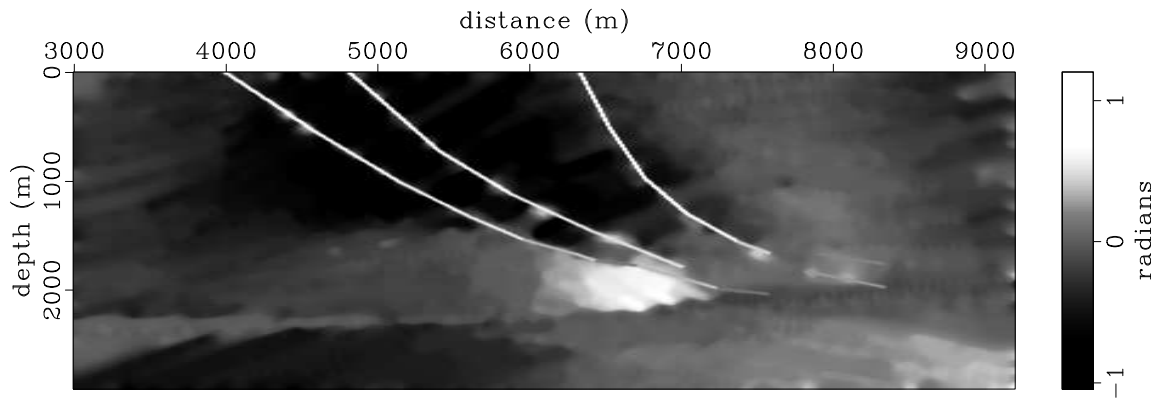


Figure 4.7: Dips derived from the migrated baseline image. These dips are used to construct the spatial regularization operator for the inversion. Note that the faults in the dip field are picked manually from the baseline image. [CR]. `chap4/. dip-0`

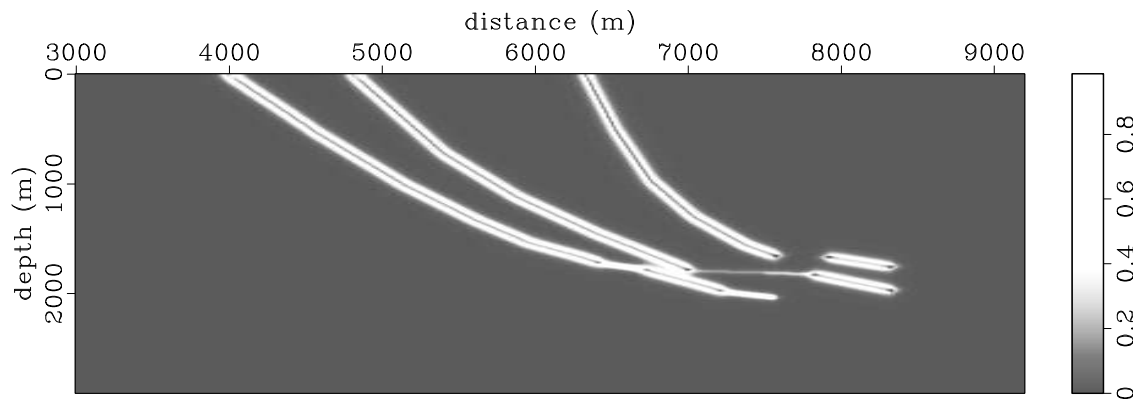


Figure 4.8: Dip-contrast computed based on how rapidly the dips change in the model. To obtain this image, the picked faults are smoothed to obtain variances based on the distance from the faults. By changing the filter range according to these variances, the faults are preserved during regularized inversion. [CR]. `chap4/. var-0`

I introduce temporal constraints into the inversion as a difference operator between the images. These constraints ensure coupling between the images during inversion, and helps with the attenuation of the incoherent crosstalk and non-repeatability artifacts between the images. In addition, temporal constrains ensure that the reflectivity changes smoothly between surveys.

Figure 4.9(a) shows the images derived from the simultaneous-source data sets by minimizing the global objective function defined in equation 4.3. These images are obtained after fifty-six conjugate gradients iterations. The corresponding time-lapse images are presented in Figure 4.9(b). A comparison of these time-lapse images with those derived from migration (Figure 4.6(b)) show that inversion has attenuated the contaminating crosstalk and non-repeatability artifacts. These time-lapse images are comparable in quality to those derived from migration of conventional data (Figure 4.5(b)). Finally, note that the inverted images in Figure 4.9 show significantly improved resolution over the migrated images derived from conventional data (Figure 4.5).

The time-lapse images derived after different numbers of iterations are presented in Figures 4.10 and 4.11. These images show how the contaminating cross-talk and non-repeatability artifacts in the time-lapse image are reduced as the number of iteration increases. For example, many of the artifacts that are present at early iterations (e.g., Figure 4.10(a)) have been attenuated after fifty iterations (e.g., Figure 4.11(b)). In this example, the cost of inverting the simultaneous data is the similar to the cost of migrating the conventional single-source data.

## **Discussion**

If the temporal spacing between seismic surveys is small, a near-continuous image of reservoir property change can be obtained (Figure 4.5). By using simultaneous sources, the acquisition cost of such seismic surveys can be reduced. Instead of being separated, the recorded data can be imaged directly with a phase-encoding operator. However, direct imaging causes crosstalk artifacts that degrade the quality of time-lapse images (Figure 4.6). Furthermore, artifacts caused by non-repeated acquisition geometries and relative shot-timings will degrade the quality of the time-lapse images (Figure 4.6(b)).

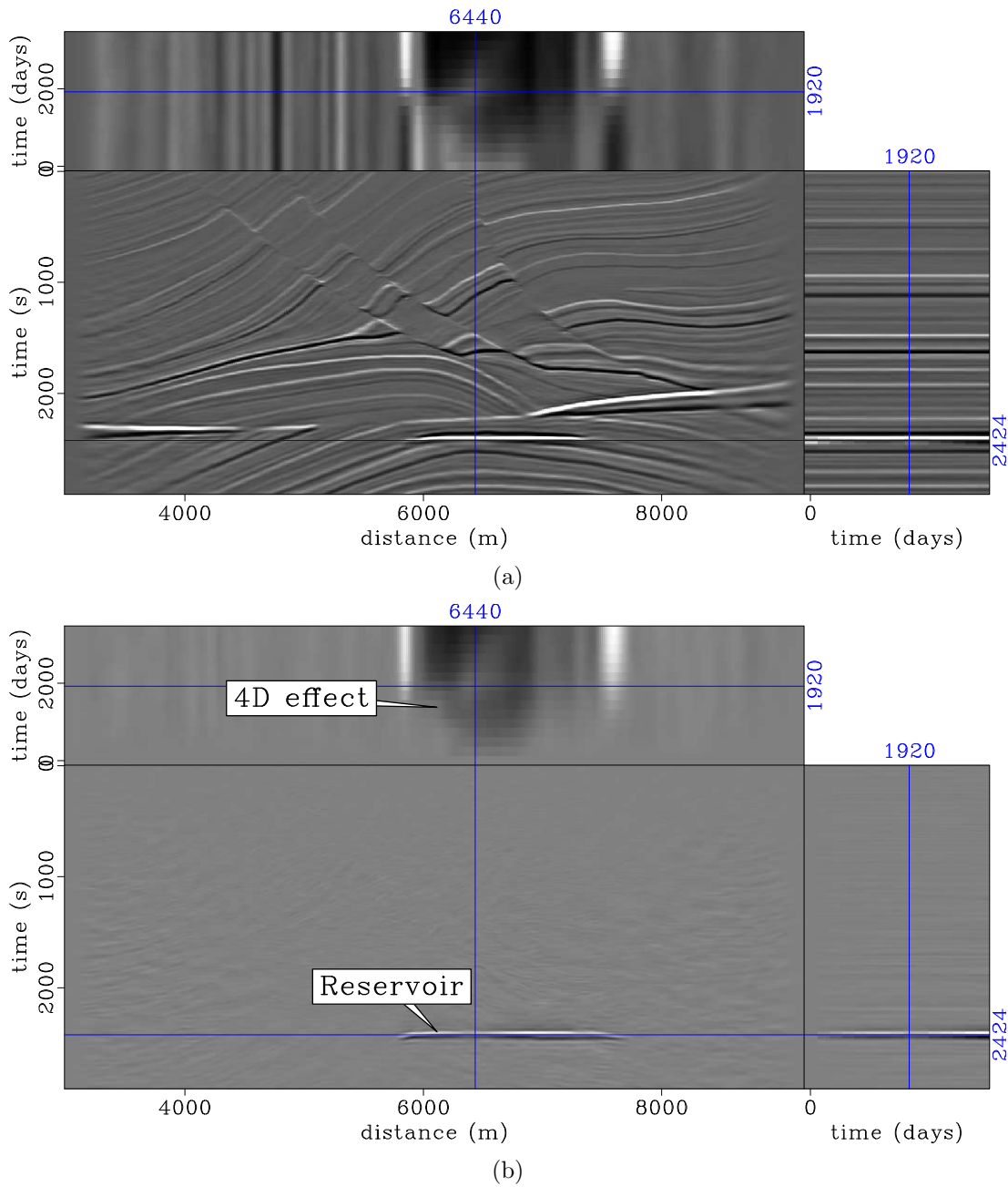


Figure 4.9: Images (a) and corresponding time-lapse estimates (b) obtained from inversion of the simultaneous-source data sets in Figure 4.3. These results are obtained after fifty-six conjugate gradients iterations. Note that the non-repeatability and crosstalk artifacts in the migrated images (Figure 4.6) have been attenuated by inversion. Also, note the improved resolution of the inverted images compared to the migrated single-source data (Figure 4.5). [CR]. `chap4/. pinv-0,pinv4d-1`

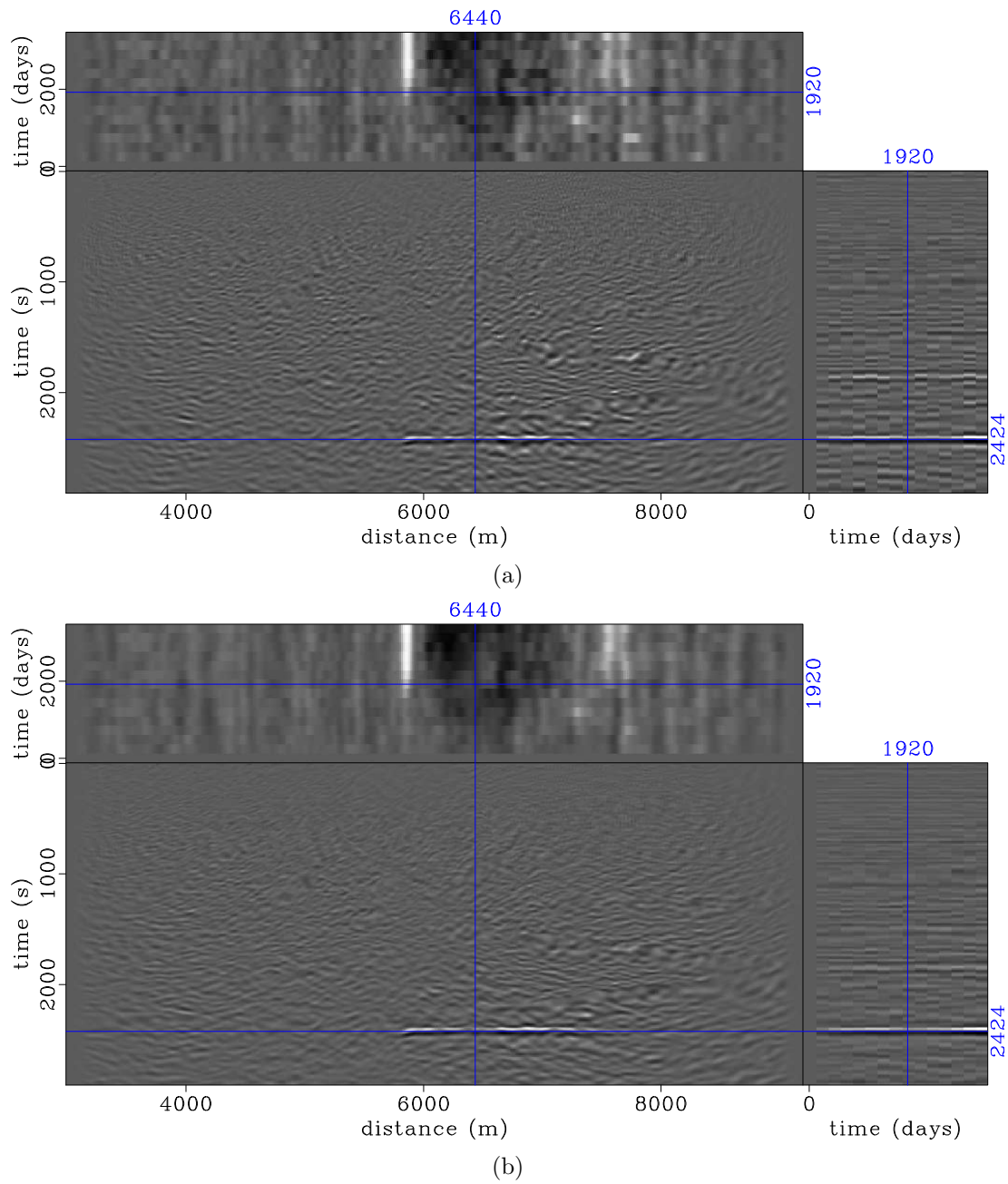


Figure 4.10: Time-lapse seismic images obtained after two and five conjugate gradient iterations (a) and (b), respectively. Note the gradual reduction in the artifacts compared to the time-lapse images from migration (Figure 4.6(b)). Furthermore, note that the artifacts have decreased in (b) compared to (a). [CR].

chap4/. pmmov4d-1,pmmov4d-2

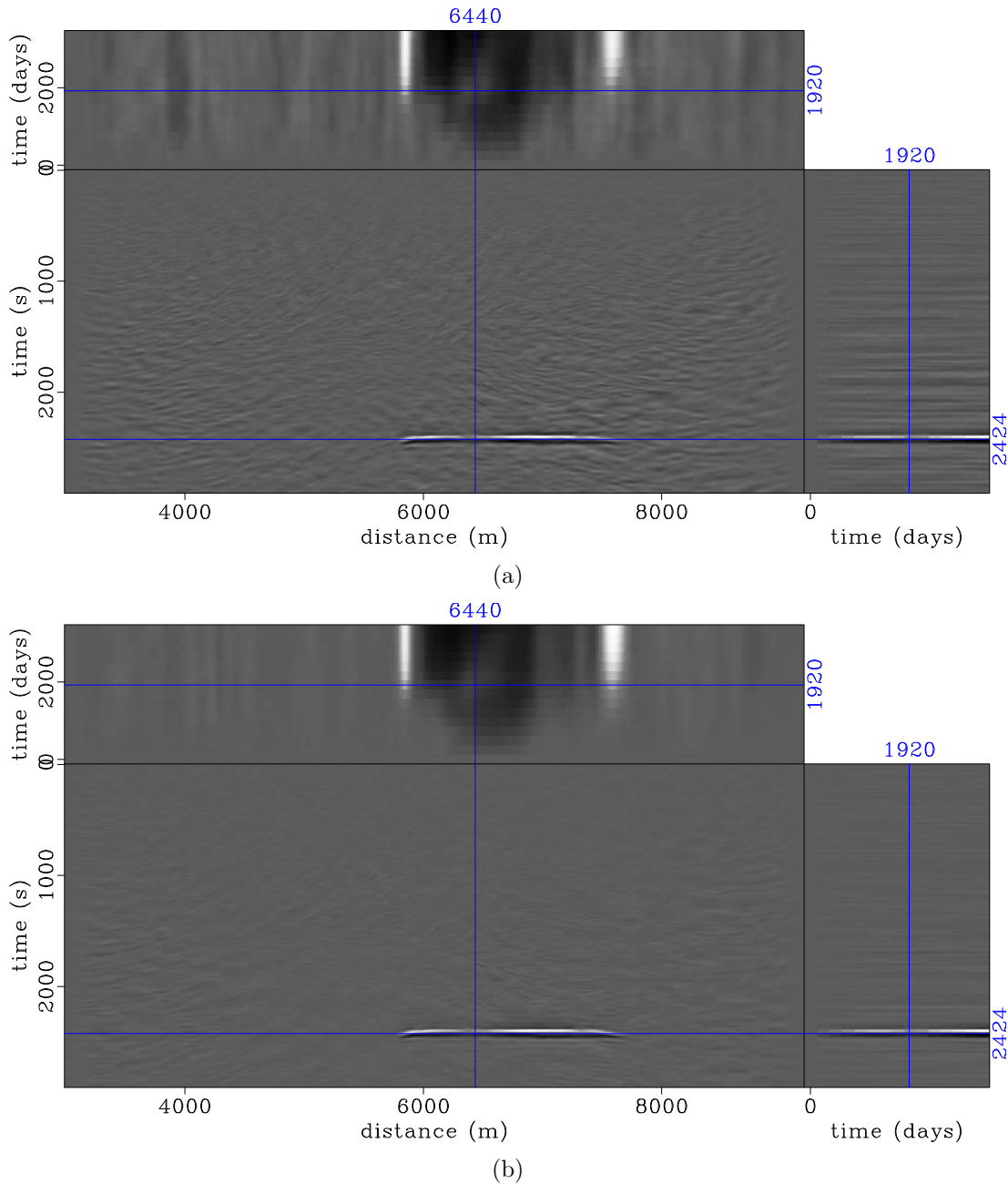


Figure 4.11: Time-lapse seismic images obtained after fifteen and fifty conjugate gradient iterations (a) and (b), respectively. Note the reduction in the artifacts compared to the time-lapse images from migration (Figure 4.6(b)). Furthermore, note that the artifacts have further decreased in (b) compared to (a) and compare to Figures 4.10(a) and 4.10(b). [CR]. `chap4/. pmmov4d-3,pmmov4d-4`

Time-lapse data sets acquired with simultaneous sources can be adequately imaged by regularized data-domain joint inversion without need for separation. Minimizing a single global objective function enables incorporation of both spatial and temporal constraints into the inversion. As shown in this example, this method attenuates both crosstalk and non-repeatability artifacts in *field-encoded* time-lapse data sets (Figure 4.9(a)). Therefore, it provides time-lapse images (Figure 4.9(b)), which are of comparable quality to those derived from perfectly repeated conventional *single-source* data sets (Figure 4.5(b)). Furthermore, images obtained from inversion of simultaneous-source data sets have higher resolution than those derived by migration of conventional single-source data sets (Figure 4.9 versus Figure 4.5). By carefully selecting both the spatial and temporal constraints, the contaminating artifacts in the time-lapse images are reduced as a function of iterations (Figures 4.10 and 4.11).

Although image-domain inversion is not easily applicable to this problem, it is more applicable than data-domain inversion to other time-lapse imaging problems. I present some of these applications in the next section.

## IMAGE-DOMAIN INVERSION

In this section, I present applications of regularized image-domain joint inversion to three synthetic examples—numbered *II* to *IV*. In example *II*, I invert for the time-lapse image below a complex salt body, correcting distortions due to complex (and irregular) illumination. Examples *III* and *IV* represent situations where surface facilities prevent data acquisition in parts of a field, thereby causing discrepancies in survey geometries. Example *III* is a two-dimensional application, while example *IV* is a three-dimensional application. Both examples show how obstruction artifacts can be attenuated by regularized joint inversion. In addition, example *IV* shows how different regularization parameters affect the quality of inverted time-lapse images. Because image-domain inversion is computationally inexpensive, an interpreter can repeat it in near real-time with various realistic constraints.

### *Example II: Inversion of sub-salt time-lapse data*

Using a single-scattering Born modeling operator, I generate two data sets over a two-dimensional sub-salt model (Figure 4.12). This model is sampled at 25 m along the horizontal axis and 10 m along the vertical axis. Each data set consists of 141 shots spaced at 50 m and 321 receivers spaced at 25 m. The maximum offset is 3000 m and the receiver spread is *rolled-along* for each shot. Apart from a change in seismic amplitudes within the reservoir, I use the same modeling parameters for both the baseline and the monitor data sets.

For reference, I also model two data sets recorded using the same geometry and the same change in reflectivity but with no salt in the overburden (Figure 4.13). In both this reference and the sub-salt models, I migrate the data sets with a shot-profile one-way wave-equation algorithm using 160 frequencies between 0.25 and 40 Hz.

The target area for inversion is indicated in both Figures 4.12 and 4.13. I compute the Hessian for the target area using 27 equally spaced frequencies within the frequency band of the data. Figure 4.14 shows the migrated monitor image, the time-lapse image, and the Hessian diagonal (subsurface illumination) for the reference, simple-overburden case (Figure 4.13). The corresponding images for the sub-salt model are presented in Figure 4.15. Note that, for the same geometry, compared to the subsurface illumination in the reference model (Figure 4.14(c)), the illumination under the complex salt body is highly irregular (Figure 4.15(c)).

The highly irregular illumination under the salt leads to inconsistent and distorted reflectivity estimates along the reservoir (Figure 4.15(a)). In addition, recall that in chapter 1, I show that because of the complex overburden, PSFs at the three closely spaced points ( $X$ ,  $Y$ , and  $Z$ ) along the reservoir in Figure 4.15(c) vary significantly in their spreading—and hence in the range of illuminated wavenumbers (Figure 1.9). Compared to the migrated time-lapse image in the simple overburden model (Figure 4.14(b)), note that the migrated time-lapse image obtained in the sub-salt model is strongly distorted (Figure 4.15(b)).

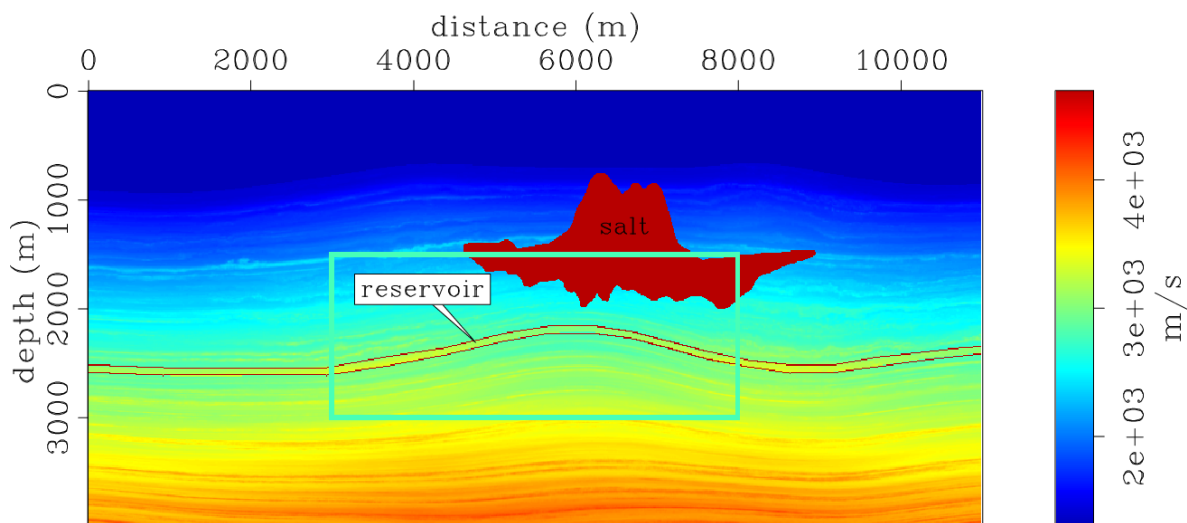


Figure 4.12: Numerical two-dimensional velocity model used in Example *II*. The box indicates the location of the target-area around the crest of the folded reservoir (top-and base indicated by the red horizon). [CR] `chap4/. sm-vel-salt-3`

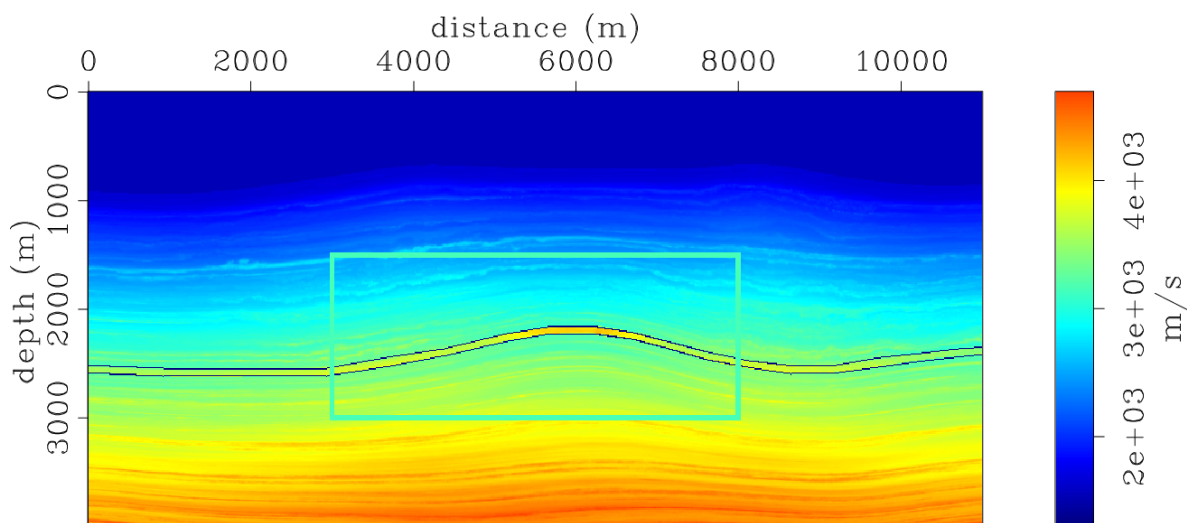


Figure 4.13: Numerical two-dimensional velocity model used to generate the reference images in Figure 4.14 and in Example *III*. The box indicates the location of the target-area around the crest of the folded reservoir (top-and base indicated by the red horizon). [CR] `chap4/. sm-vel2`

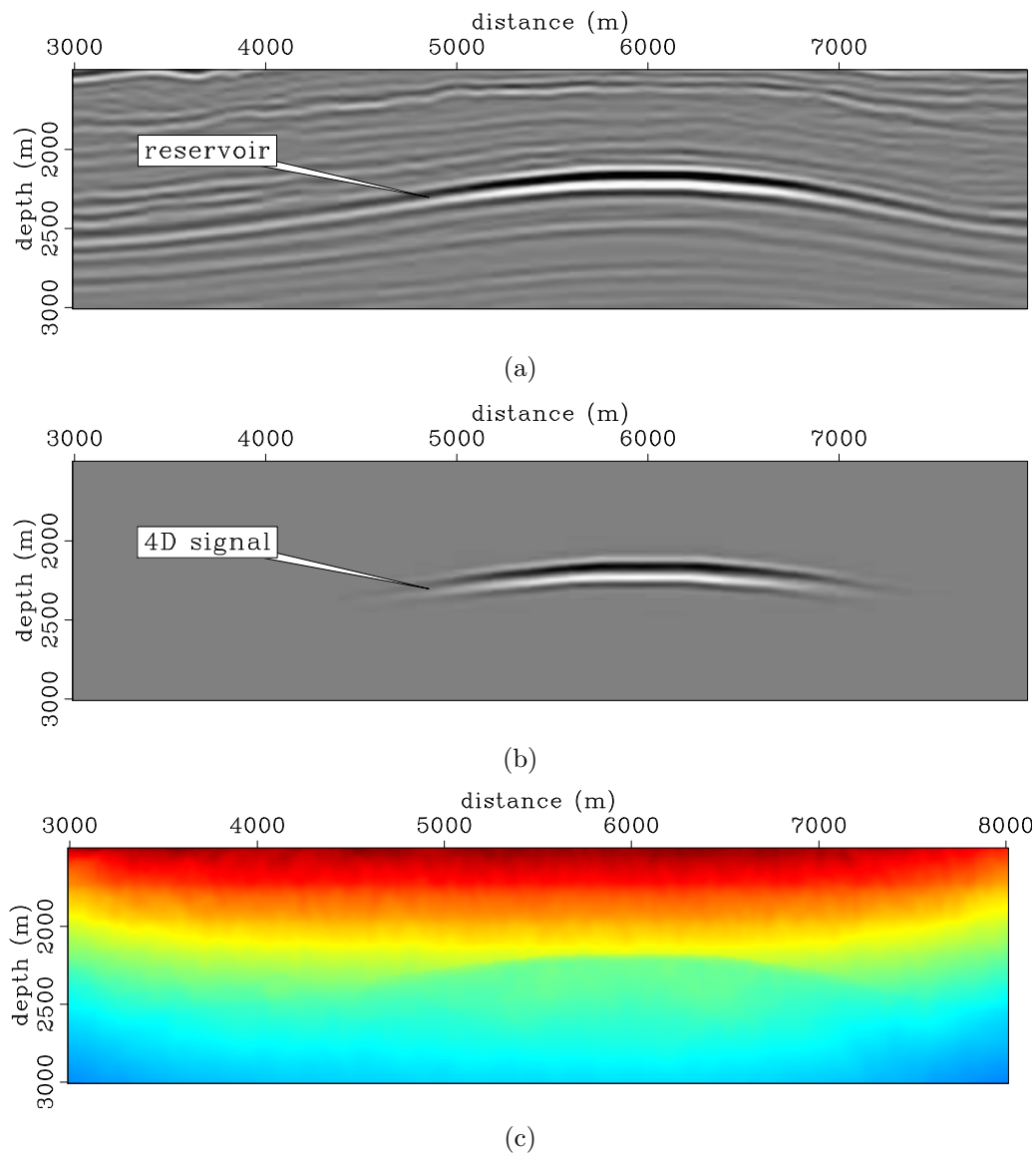


Figure 4.14: Migrated monitor (a) and time-lapse (b) images, and subsurface illumination (c) for the target area shown in Figure 4.13. In (c), red indicates high illumination, whereas blue indicates low illumination. Compare these images to those in Figures 4.15 and 4.18. [CR] chap4/. s-mig-2l,s-mig-dl,s-dhes

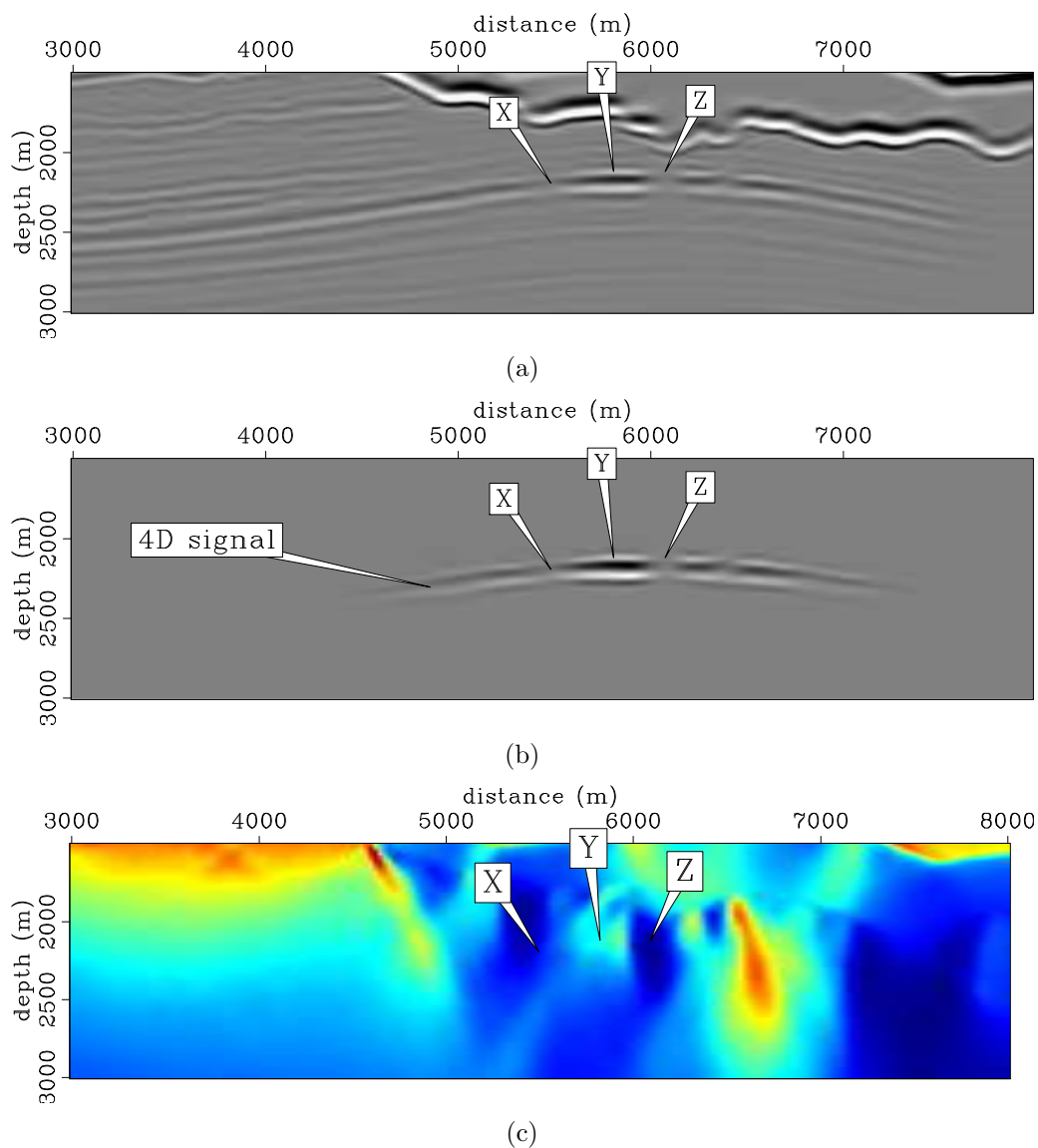


Figure 4.15: Migrated monitor (a) and time-lapse (b) images, and subsurface illumination (c) for the target area shown in Figure 4.12. At points  $X$ ,  $Y$ , and  $Z$  along the reservoir, note that the illumination is highly irregular, the migrated image is distorted, and compared to Figure 4.15(b), the time-lapse image is distorted. Recall that point-spread-functions at points  $X$ ,  $Y$ , and  $Z$  are shown in Figure 1.9. [CR] chap4/. s-mig-salt-2l,s-mig-salt-dl,s-dhes-saltl

Prior to inversion, to simulate incoherent noise between the surveys, I add 5% uniformly distributed random noise to each data set. The monitor and time-lapse images derived from regularized joint inversion of the reference data are presented in Figure 4.16. The corresponding inverted images derived from the sub-salt data are presented in Figure 4.17.

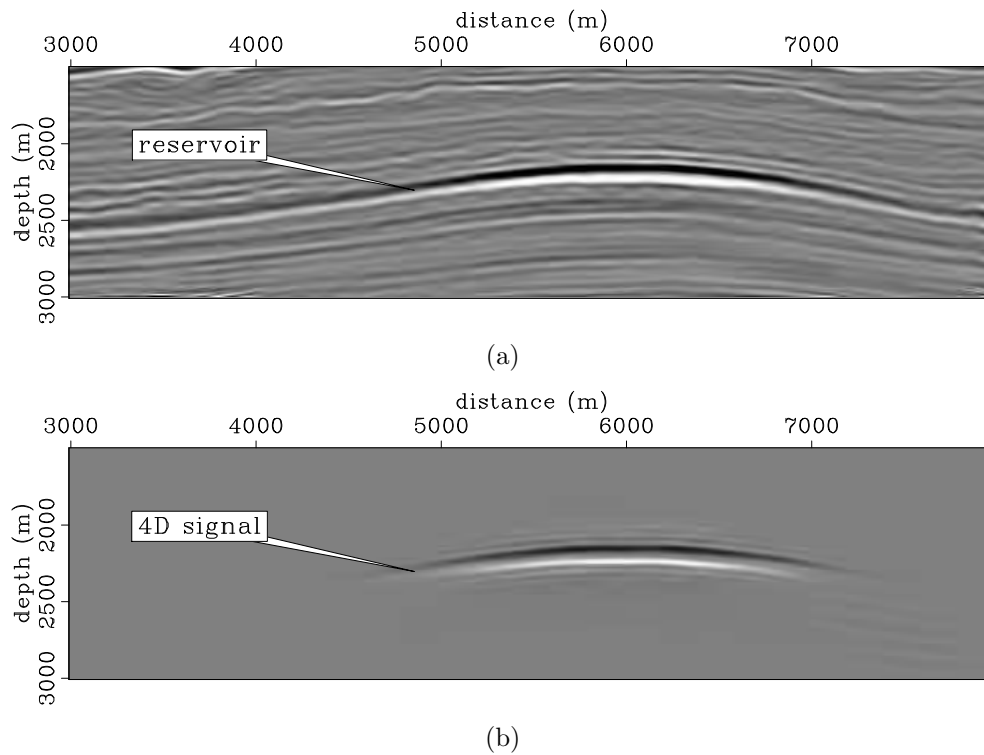


Figure 4.16: Inverted monitor (a) and time-lapse (b) images for the target area shown in Figure 4.13. Note that these images show improved resolution over the migrated images (Figure 4.14). Compare these to the inverted images in Figures 4.17 and 4.19. [CR] chap4/. s-inv-2l,s-inv-dl

Compared to the migrated reference images (Figure 4.14), the inverted reference images show improved resolution. Importantly, the distortions present in the migrated time-lapse image (Figure 4.15(b)) have been corrected in the inverted time-lapse image (Figure 4.17(b)). The subs-salt time-lapse image derived from regularized inversion is of comparable quality to that derived from the reference model (Figure 4.16(b)).

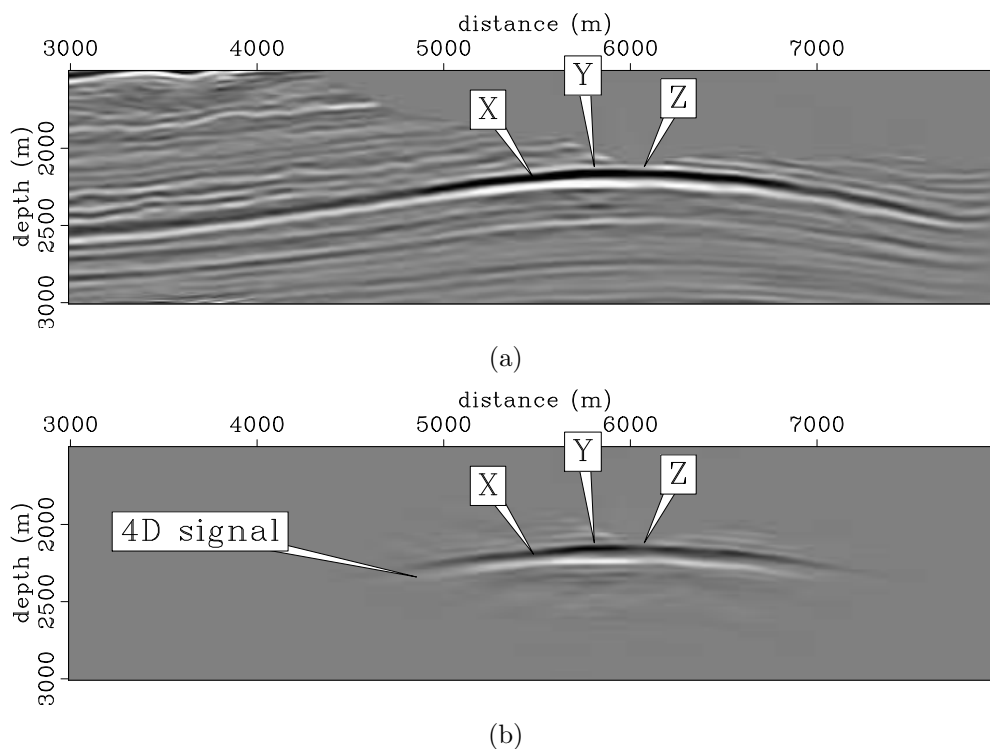


Figure 4.17: Inverted monitor (a) and time-lapse (b) images for the target area shown in Figure 4.12. Note that these images are comparable to those in Figure 4.16. Importantly, at points  $X$ ,  $Y$ , and  $Z$ , note that distortions in the migrated time-lapse image (Figure 4.15(b)) have been corrected by inversion. The salt body in these images has been cropped for clarity. [CR] `chap4/. s-inv-salt-2l,s-inv-salt-dl`

## Discussion

Conventional imaging with a migration operator is sufficient to image targets when the overburden is simple and where survey geometries are repeated for the baseline and monitor surveys (Figure 4.14). This is because, in such a case, the reservoir is sufficiently illuminated (Figure 4.14(c)) and migration is a good approximation to the inverse. However, where the reservoir overburden is complex, the subsurface illumination becomes highly irregular and the migrated image—and as a consequence the time-lapse image—is strongly distorted (Figure 4.15). This distortion results from

the high variability in the sets of angles at which points along the reservoir are illuminated (Figure 1.9). In this case, migration is a poor approximation to the inverse of the linearized seismic modeling operator.

Regularized image-domain inversion provides a way to remove the band-limited wave-propagation effects through the complex reservoir overburden. As shown in this example, even for the simple overburden example, image-domain inversion provides time-lapse images with better resolution compared to migration (Figure 4.16(b)). In the complex overburden example, inversion corrects for the distortions in the migrated image (Figure 4.17(a)), and consequently in the time-lapse image (Figure 4.17(b)). Importantly, whereas the time-lapse reflectivity images obtained from migration are different for the simple and complex overburden examples (Figure 4.14(b) versus Figure 4.15(b)), those from inversion are similar (Figure 4.16(b) versus Figure 4.17(b)). Therefore, with image-domain inversion, the time-lapse reflectivity image becomes less sensitive to the overburden complexity.

### *Example III: Inversion of incomplete data - 2D example*

In this example, using the same modeling parameters as in example *II*, I generate two data sets along the reference model in Figure 4.13. However, to simulate an obstruction in the monitor data, I create a 400 m and a 1200 m hole along the shot and receiver axes, respectively.

Figure 4.18 shows the migrated monitor image, the time-lapse image and the subsurface illumination for the target area. In Figure 4.18(b), note that compared to the reference time-lapse image (Figure 4.14(b)), the time-lapse amplitudes are contaminated by the obstruction artifacts. Recall that in chapter 1, I show that because of the differences in acquisition geometries, PSFs at the image point on reservoir marked in Figure 4.18 vary significantly in their spreading and range of illuminated wavenumbers (Figure 1.8).

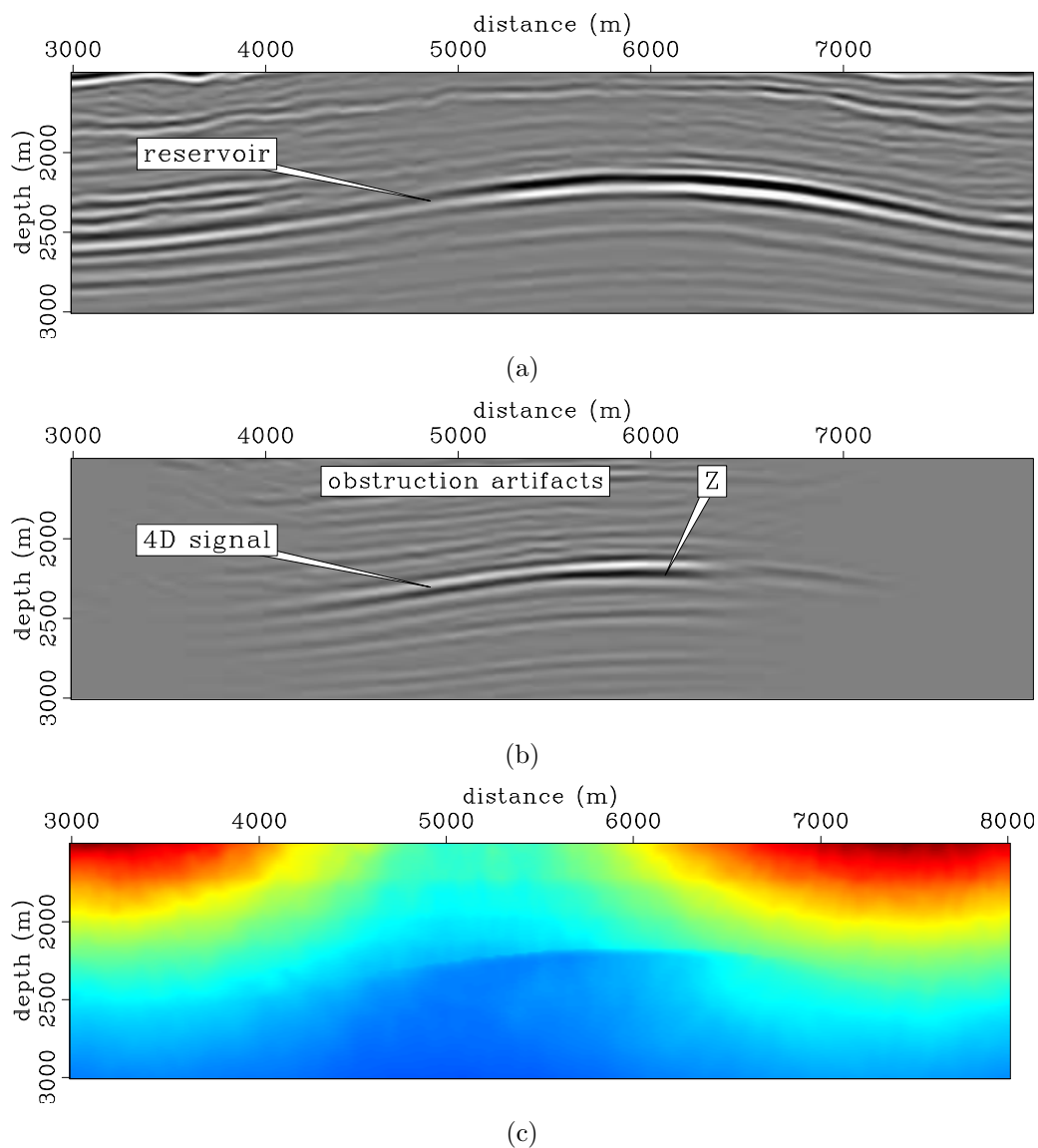


Figure 4.18: Migrated monitor image (a), time-lapse image (b), and subsurface illumination (c) for the target area shown in Figure 4.13, where an a simulated obstruction causes a gap in the monitor data. Note that, compared to the reference time-lapse image (Figure 4.14(b)), the time-lapse image (b) is contaminated by obstruction artifacts. The difference in the point-spread-functions for the baseline and monitor geometries at point  $Z$  is shown in Figure 1.8. [CR] chap4/. s-mig-gap-2l,s-mig-gap-dl,s-dhes-gap

The monitor and time-lapse images derived from regularized joint inversion are presented in Figure 4.19. Note that the obstruction artifacts in the migrated time-lapse image (Figure 4.18(b)) have been attenuated by inversion (Figure 4.19(b)), thereby providing a time-lapse image of comparable quality to the reference model (Figure 4.16(b)).

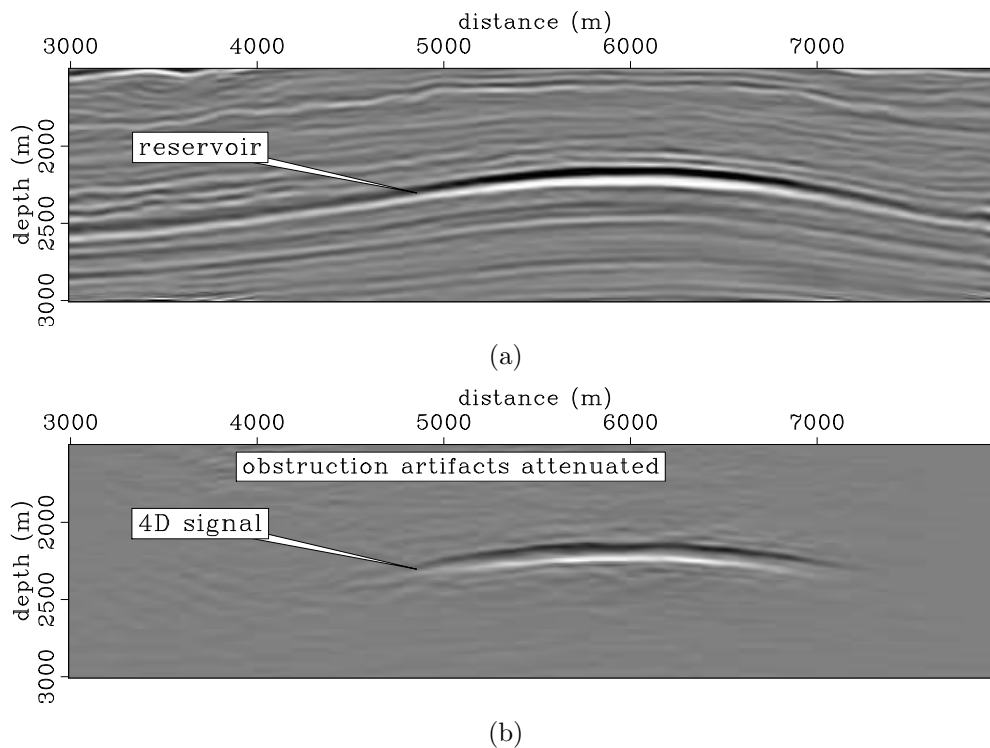


Figure 4.19: Inverted monitor (a) and time-lapse (b) images for the target area shown in Figure 4.13 with a simulated obstruction in the monitor data. Note that these images are comparable to those in Figure 4.16. [CR] chap4/. s-inv-gap-2l,s-inv-gap-dl

### Discussion

Differences in the acquisition geometries of time-lapse seismic surveys result in artifacts that can mask reflectivity change of interest (Figure 4.18). Such artifacts result because the migration operator cannot fully account for differences in the acquisition geometries. As in Example II, in this example, migration is a poor approximation

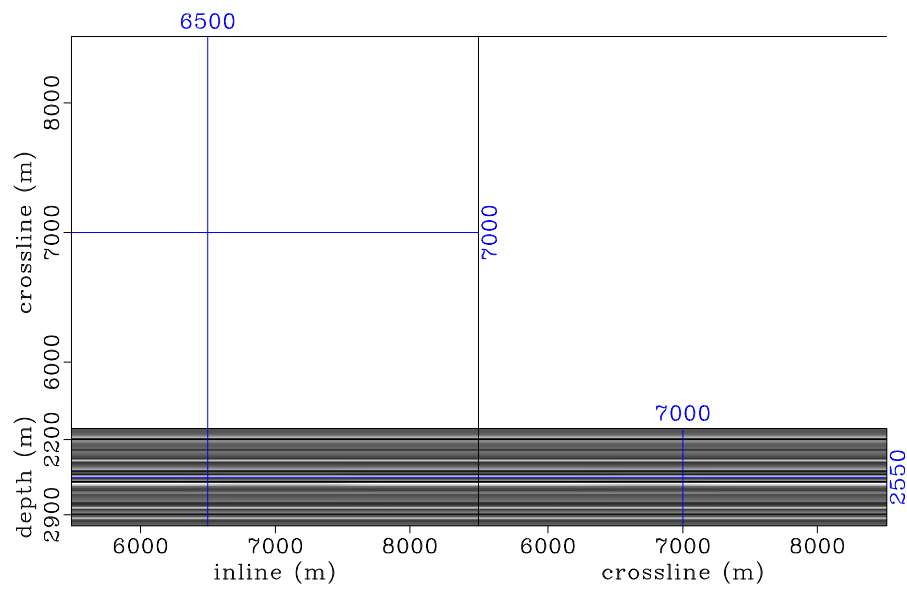
to the inverse of the linearized seismic modeling operator.

Regularized image-domain inversion provides a way to account for differences in acquisition geometries between time-lapse surveys. As shown in Figure 4.19(b), the inverted time-lapse image is comparable in quality to that obtained from for the perfectly repeated geometries (Figure 4.16(b)). Furthermore, the time-lapse image in this example (Figure 4.19(b)) is comparable to the one derived in the sub-salt example (Figure 4.17(b)). Therefore, regularized image-domain inversion makes the time-lapse image less sensitive to the overburden complexity—as shown in example *II*—and to the differences in acquisition geometries—as shown in this example.

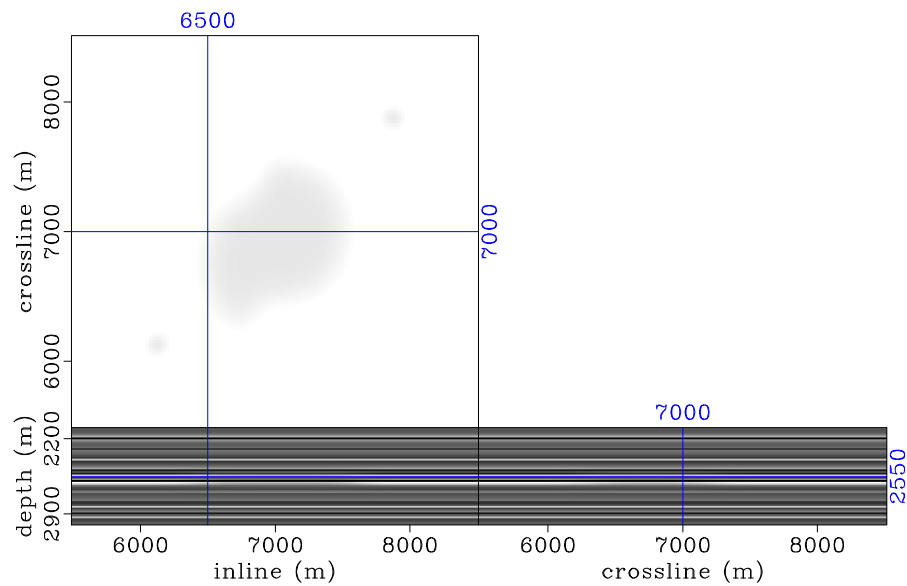
#### *Example IV: Inversion of incomplete data - 3D example*

In this example, I simulate three migrated images by convolving the Hessian matrices of three OBC field-data geometries (discussed in detail in chapter 6) with carefully designed time-lapse reflectivity models. The reflectivity models consist of horizontally-layered events with both positive and negative time-lapse amplitude changes. I assume expanding regions of change in the seismic amplitudes of opposite polarities along the top and bottom of the reservoir. In addition, I assume that the reservoir is faulted, causing strike-slip displacement of the central time-lapse amplitudes.

The baseline reflectivity (not shown) is constant along each reflectors. Figure 4.20 shows band-limited versions of the two monitor reflectivity models. Figure 4.21 shows the time-lapse amplitudes obtained by subtracting the reference baseline image from the two reference monitor images (Figure 4.20). As discussed in chapter 6, whereas the baseline is modeled with a complete geometry, the two monitor geometries contain different sizes of overlapping gaps. The simulated migrated time-lapse images are shown in Figure 4.22. Note that, because of the differences in the acquisition geometries, compared to the *true* reflectivity images (Figure 4.21), these time-lapse images are strongly contaminated.

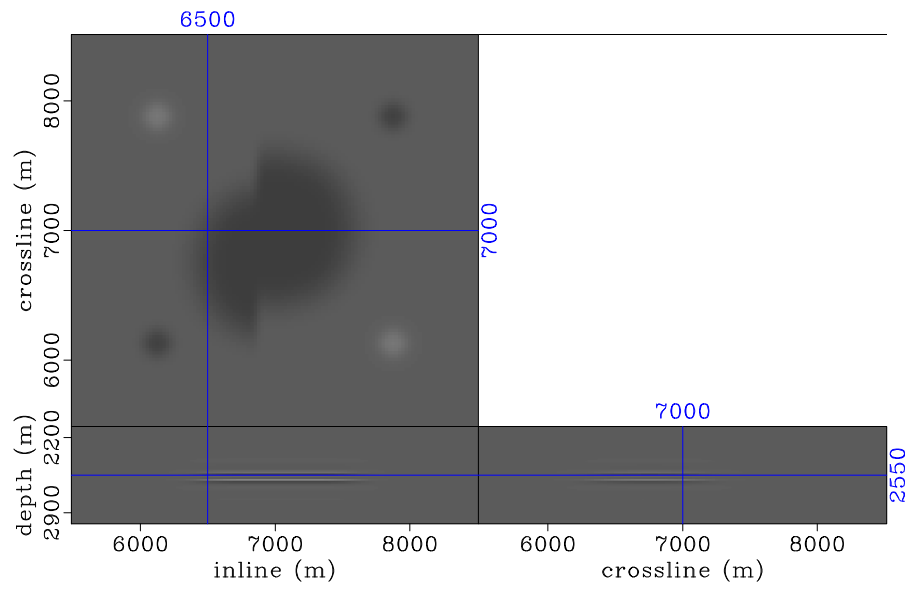


(a)

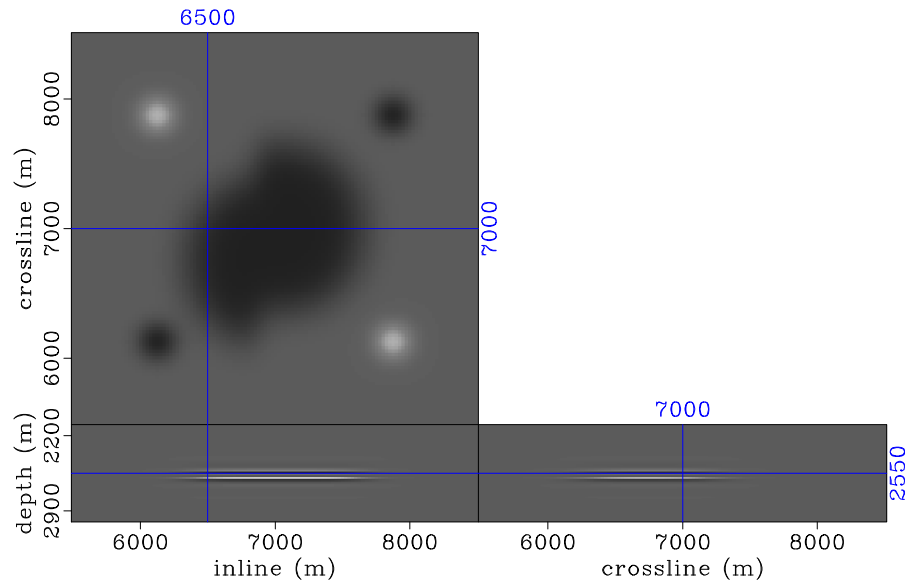


(b)

Figure 4.20: Band-limited reference reflectivity models for the first (a), and second (b) monitors. The baseline model is similar to these but with constant reflectivity along each horizontal reflector. The reference time-lapse models computed as the differences between (a) and (b), and the baseline reflectivity model are shown in Figure 4.21. [CR]. chap4/. ref-2,ref-3

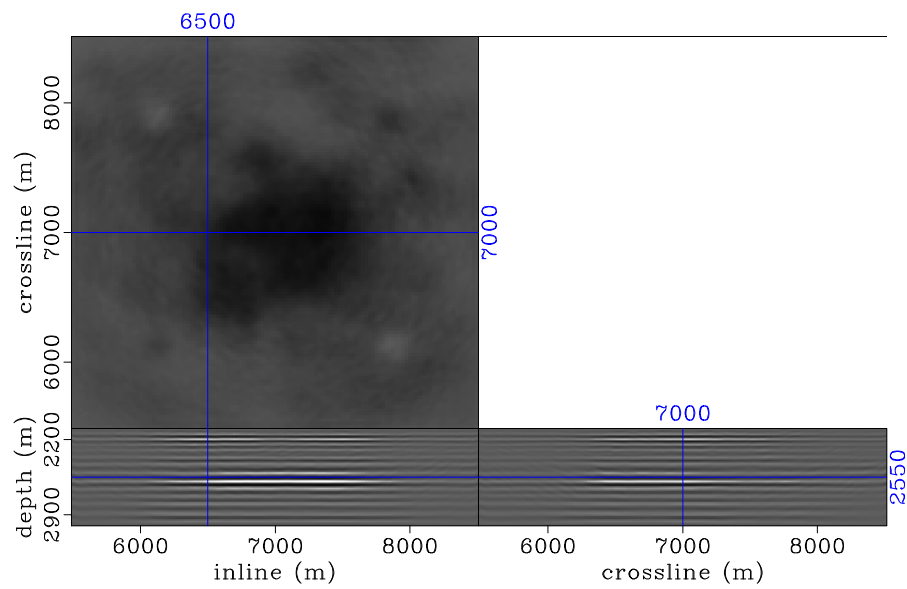


(a)

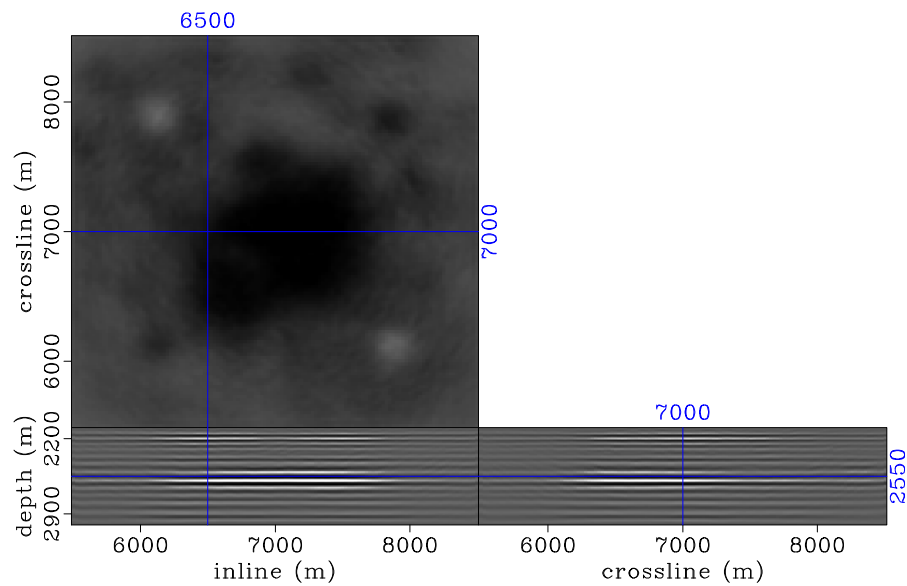


(b)

Figure 4.21: Reference time-lapse images between the first (a), and second (b) monitor models (Figure 4.20) and the baseline model (not shown). Note that reflectivity changes increase in amplitude and size with time. [CR]. chap4/. ref-d1,ref-d2



(a)



(b)

Figure 4.22: Migrated time-lapse images between the first (a), and second (b) synthesized monitor images and the baseline. Note that, compared to the reference time-lapse images (Figure 4.21), the time-lapse amplitudes are contaminated by obstruction artifacts. [CR]. `chap4/. smig-d1,smig-d2`

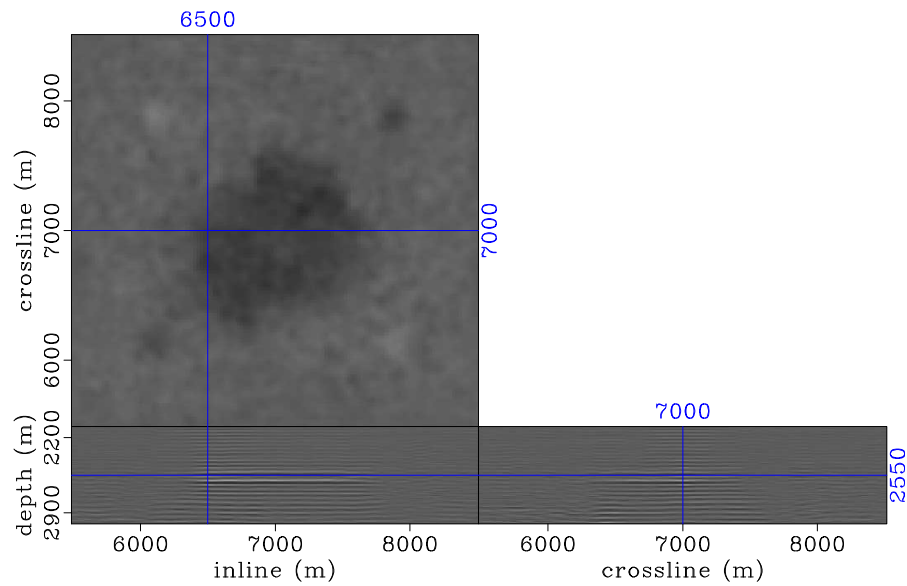
The time-lapse images obtained by inversion with weak coupling between the images are shown in Figure 4.23. This is equivalent to inverting the images separately. Note that, although the time-lapse images are improved, they still contain several artifacts absent in the reference model (Figure 4.21). The inverted time-lapse images derived using the same spatial regularization parameters as in Figure 4.23, but temporal coupling that is too strong are shown in Figure 4.24. Note that although artifacts have been reduced in the images, the time-lapse amplitudes have also been destroyed.

Figure 4.25 shows the inverted time-lapse images derived using the same spatial regularization parameters as in Figures 4.23 and 4.24, but intermediate temporal coupling between the image. Note that the time-lapse images obtained in this case are comparable in quality to the reference time-lapse models (Figure 4.21).

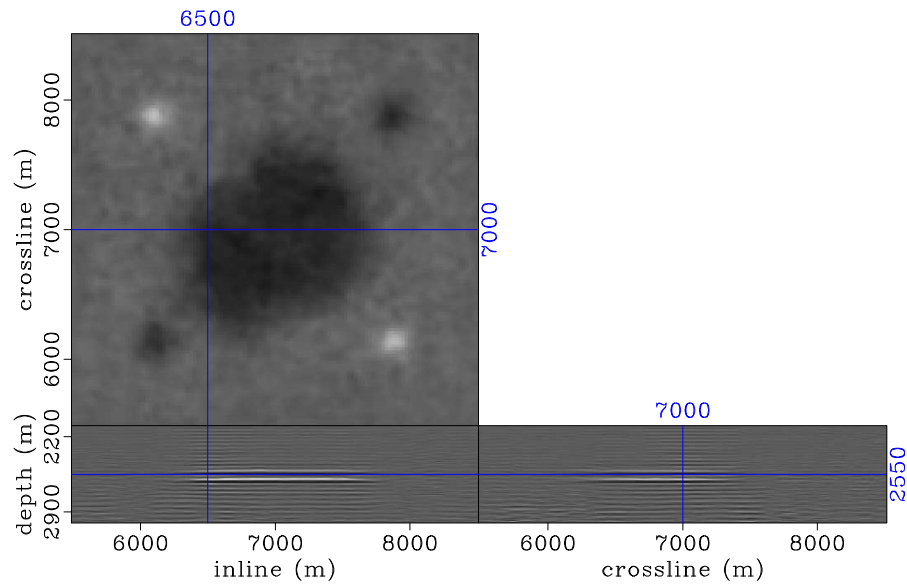
## Discussion

As discussed earlier, because linearized inversion of time-lapse seismic data sets is an ill-posed problem, it is often necessary to regularize it. Therefore, the choice of regularization operators and parameters is an important component of solving this problem. As demonstrated in this and previous examples, solving this inversion jointly enables incorporation of spatial and temporal regularization. In practice, because it is usually difficult to determine the optimum regularization parameters prior to inversion, it is usually necessary to test different parameters. An important advantage of image-domain inversion is that once the approximate Hessian is precomputed, it can be reused for different regularization parameters.

In this example, artifacts in the migrated time-lapse images (Figure 4.22), resulting from differences in acquisition geometries, can be attenuated by inversion weakly-coupled (Figure 4.23). However, because this is similar inverting the images separately, it is difficult to obtain temporally-consistent inverted images. Therefore, differences in residual artifacts between these *separately-inverted* images still contaminate the inverted time-lapse images.



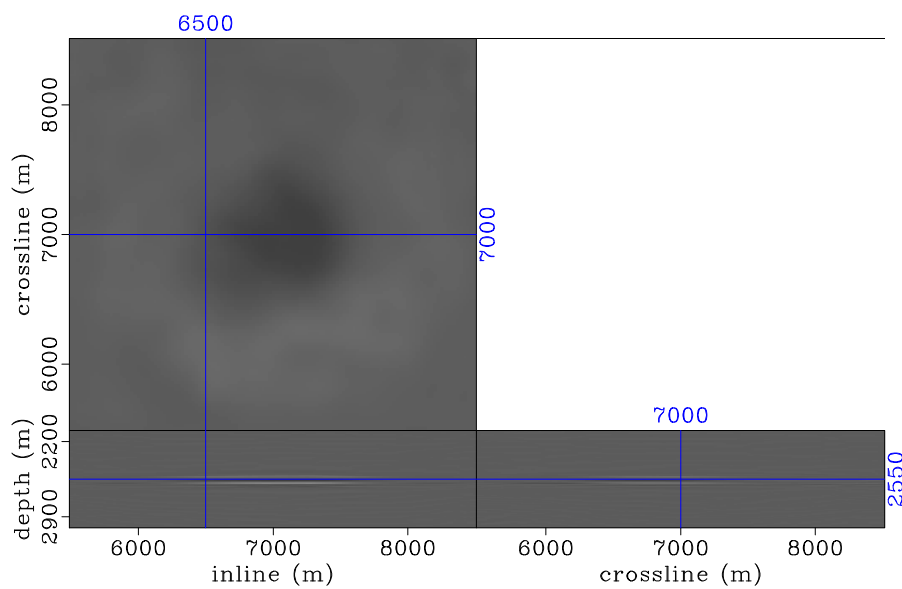
(a)



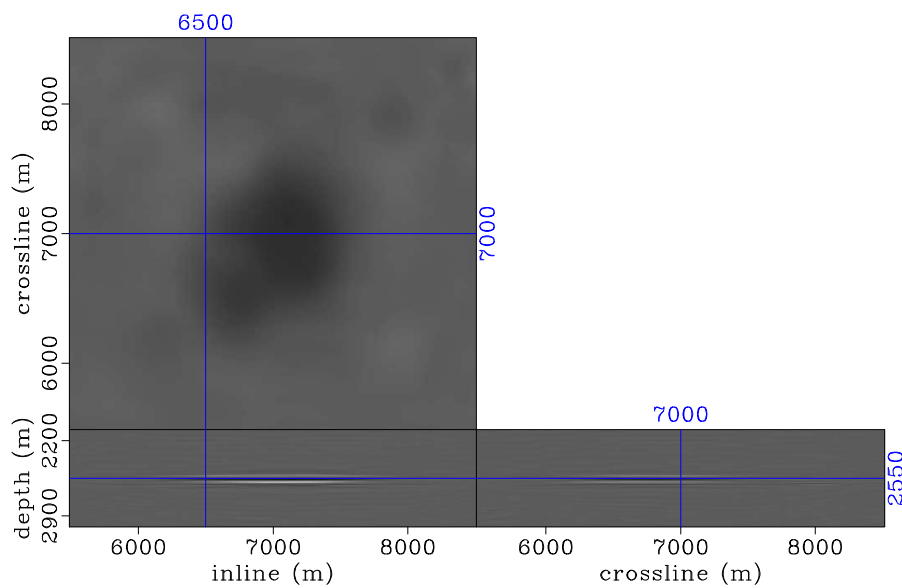
(b)

Figure 4.23: Inverted time-lapse images between the first (a), and second (b) monitor and the baseline, derived from weakly-coupled joint inversion between the baseline and monitor images. Note that, although most of the obstruction artifacts in Figure 4.22 have been attenuated, the time-lapse amplitudes are still contaminated by numerous artifacts not present in the reference time-lapse images (Figure 4.21).

chap4/. small-d1,small-d2

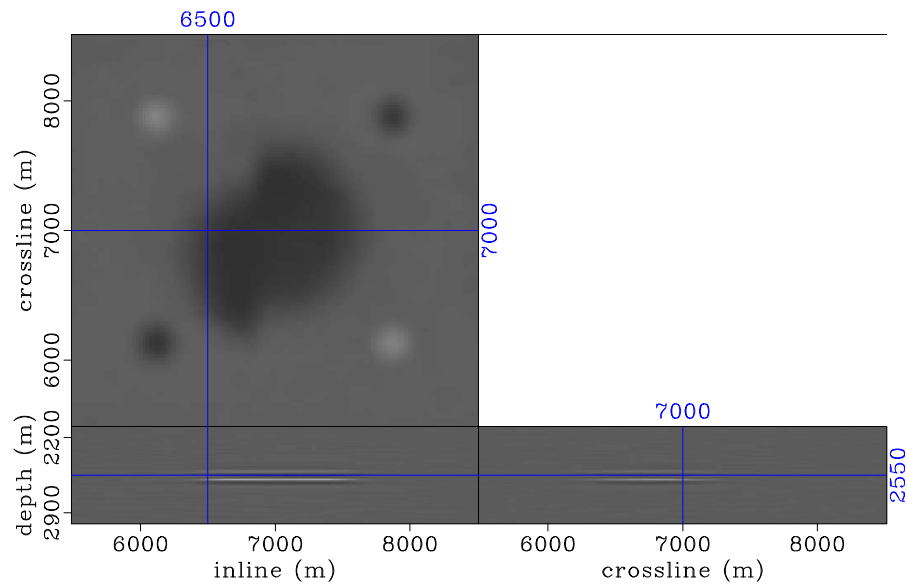


(a)

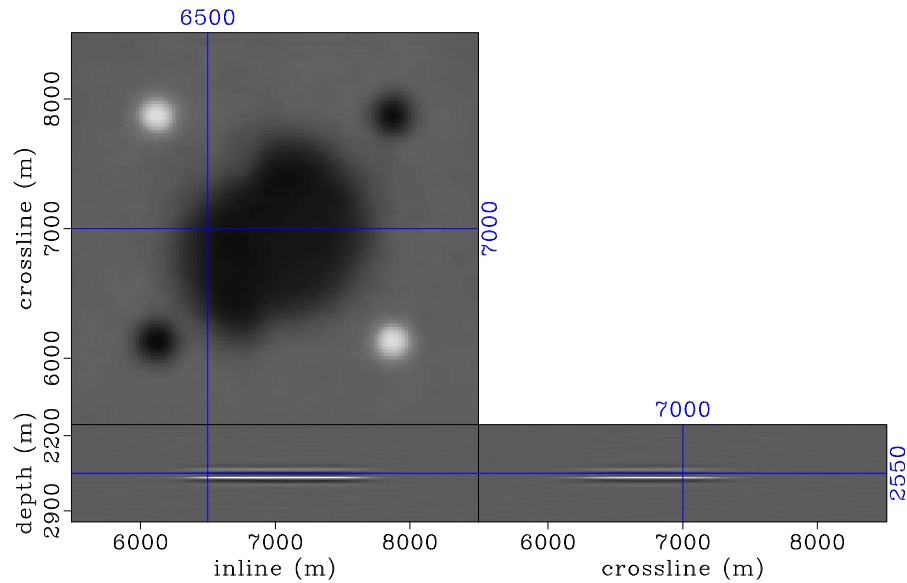


(b)

Figure 4.24: Inverted time-lapse images between the first (a), and second (b) monitor and the baseline derived from strongly-coupled joint inversion between the baseline and monitor images. Note that, although the artifacts in Figures 4.23 and 4.22 have been attenuated, compared to the reference time-lapse images (Figure 4.21), the time-lapse amplitudes have been destroyed. chap4/. high-d1,high-d2



(a)



(b)

Figure 4.25: Inverted time-lapse images between the first (a), and second (b) monitor and the baseline, derived from satisfactorily coupled joint inversion of the baseline and monitor images. Note that the obstruction artifacts are sufficiently attenuated, whereas the time-lapse amplitudes are preserved. These results are comparable in quality to the reference time-lapse images (Figure 4.21). chap4/. med-d1,med-d2

Using a temporal regularization parameter that is too large leads to too-strong coupling between the inverted images. As noted above, although strong temporal coupling attenuates differences in residual artifacts between images, it also destroys the time-lapse reflectivity of interest (Figure 4.24). By using a temporal regularization parameter that sufficiently couples the inverted images without destroying the time-lapse reflectivity, it is possible to obtain time-lapse images (Figure 4.25), which are comparable to the reference images (Figure 4.21).

## CONCLUSIONS

In this chapter, I have demonstrated applications of regularized joint inversion in the data domain and in the image domain. I showed that by inverting field-encoded data acquired with simultaneous sources, it is possible to attenuated artifacts caused by geometry and shot-time non-repeatabilities. This approach can speed up both seismic acquisition and imaging and may make possible near-continuous monitor of reservoirs. Another application of data-domain joint inversion is in the least-squares imaging of conventional time-lapse data, where computer-base encoding is applied to individual *single-source* data sets.

In addition, I showed how distortions in time-lapse images caused by complex overburden can be attenuated by regularized joint image-domain inversion. Furthermore, I showed regularized joint image-domain inversion can be used to attenuate artifacts in time-lapse images caused by obstructions in time-lapse seismic acquisition surveys. These examples demonstrate that it is possible to obtain reliable time-lapse images that are independent of overburden complexity and differences in seismic acquisition geometries.

Lastly, using a three-dimensional example, I showed how the choice of regularization parameters affect the inverted time-lapse image. Without coupling between the inverted images, because the inverse problem is ill-posed, it is difficult to obtain reliable time-lapse images. However, if the temporal coupling is too strong, the time-lapse amplitudes of interest may become destroyed. Image-domain inversion

requires pre-computation of an approximate *truncated* Hessian matrix of the least-squares objective function. Once this matrix is computed, image-domain inversion is relatively cheap. Therefore it is possible to try several regularization parameters until satisfactory results are obtained.

In chapters 5 and 6, I show applications of regularized joint image-domain inversion to two- and three-dimensional field data sets.

## ACKNOWLEDGEMENTS

The original Marmousi velocity model, which was modified and used to synthetic models in example *I*, was provided by Institut. Franais du Petrole (IFP). I thank SEG for providing the SEAM model, from which the two-dimensional models in examples *II* and *III* are extracted and modified. The Hessian matrices in example *IV* were generated using velocity models and data geometries modified from the Valhall Life-of-Field-Seismic data sets provided by BP.